Characterization and Mitigation of Dimensional Effects on Core Loss in High-Power High-Frequency Converters

Ahmed Nabih, *Member, IEEE*, Feng Jin, *Student Member, IEEE*, Rimon Gadelrab, *Member, IEEE*, Fred. C. Lee, *Life Fellow, IEEE*, and Qiang Li, *Member, IEEE*

***Abstract*—To date, LLC resonant converters have been deployed in many applications for improved efficiency, density, and reliability. With the introduction of wide-bandgap devices coupled with the soft switching feature, the switching frequency can be extended beyond megahertz. With the significant increase in operating frequency, complicated magnetic components can be broken down into a cellular structure, each with a few number of turns. They can be easily implemented using four to six layers of printed circuit board windings. Moreover, integrating the cellular cores using flux cancellation can further improve the power density. The proposed integrated magnetics can be automated in the manufacturing process. With the recently developed high-frequency core material, phenomena referred to as the dimensional effects on core loss are observed. The dimensional effects are discussed in the literature when using an unusually large core structure; however, at high excitation frequencies, it can be observed more frequently, particularly with integrated magnetic components. In this article, we give an overview of the dimensional effects on core loss, namely flux crowding, dimensional resonance, and eddy loss, with the latest being a dominant factor in the 1-MHz transformer loss. We also introduce a practical method for the characterization of the dimensional effects to help engineers better design their high-frequency converter. This includes measuring the ferrite material characteristics and evaluating the dimensional effects using finite-element analysis. Finally, a case study of 1-MHz 400-to-48 V converter design is presented, showing superiority in both power density and efficiency metrics compared to other reported literature from the same category. This shows the importance of including the dimensional effects and, specifically, the core eddy loss in the design procedure.**

***Index Terms*—Data center, high frequency, LLC converter, matrix inductor, matrix transformer, printed circuit board (PCB) magnetics, wide bandgap, 48-V bus architecture.**

Manuscript received 7 February 2023; revised 14 April 2023; accepted 3 June 2023. Date of publication 13 June 2023; date of current version 22 September 2023. This work was supported by the Power Management Consortium. Recommended for publication by Associate Editor D. Dujic. *(Corresponding author: Qiang Li.)*

Ahmed Nabih and Rimon Gadelrab were with the Center for Power Electronics Systems CPES, Virginia Tech, Blacksburg, VA 24061 USA. They are now with Texas Instruments, Inc., Dallas, TX 75243 USA (e-mail: ahmed-nabih@ti.com; rimon@ti.com).

Feng Jin, Fred. C. Lee, and Qiang Li are with the Center for Power Electronics Systems CPES, Virginia Tech, Blacksburg, VA 24061 USA (e-mail: fengjin@vt.edu; fclee@vt.edu; lqvt@vt.edu).

Color versions of one or more figures in this article are available at https://doi.org/10.1109/TPEL.2023.3285633.

Digital Object Identifier 10.1109/TPEL.2023.3285633

I. Introduction

THE key performance attributes in today's power electronics industry are efficiency, density, reliability, and cost. The manufacturing process is labor intensive. Resonant converters, such as LLC and $CLLC$, have been intensively studied and applied in many applications, such as data centers and telecom power supplies, electric vehicle (EV) chargers, TV panels, and LED drivers. The evolution in clean energy transportation, artificial intelligence, and the Internet of Things has been accelerating for the past few years. Consequently, the EV charger and data center power supply markets are surging. The EV charger points are growing annually with an average growth rate of 50% [1]. According to a report from *Nature* magazine [2], the total electricity consumption of the information and communication technology sector is projected to reach 8000 TWh by 2030, accounting for around 20% of global electricity consumption. These trends have motivated efforts to improve the cost efficiency and performance of power architecture in these applications. Fig. 1 shows the power architecture for the EV charging and the 48-V data center architecture involving ac–dc and dc–dc power converters. Moving to higher voltage dc–dc converters has been proven beneficial in both the applications. Moving from 400 to 800 V charging in the EV doubles the charging speed, offering higher recharging power without compromising the I^2R losses [3]. Similarly, moving from a 12 to a 48-V bus in the data center architecture delivers four times the power with the same I^2R loss on the bus [4]. The scope of this article is to assess the implications of the higher voltage power delivery on the high-frequency dc–dc design and performance, particularly on the magnetic core size and loss. With the advent of wide-bandgap devices and soft switching topologies, the power electronic converters are breaking new grounds in terms of efficiency and power density by pushing the switching frequency by a fact of 10×, up to the megahertz range [5], in comparison with its silicon counterpart. At this frequency, the magnetic size is reduced, and planar magnetics using printed circuit board (PCB) winding become more relevant. PCB magnetics feature multiple advantages over Litz wire. The benefits are summarized as follows.

1) The labor-intensive manufacturing process can be automated; thus, there is a reduction of cost.
2) There is much reduced common-mode noise by using the shield layer.

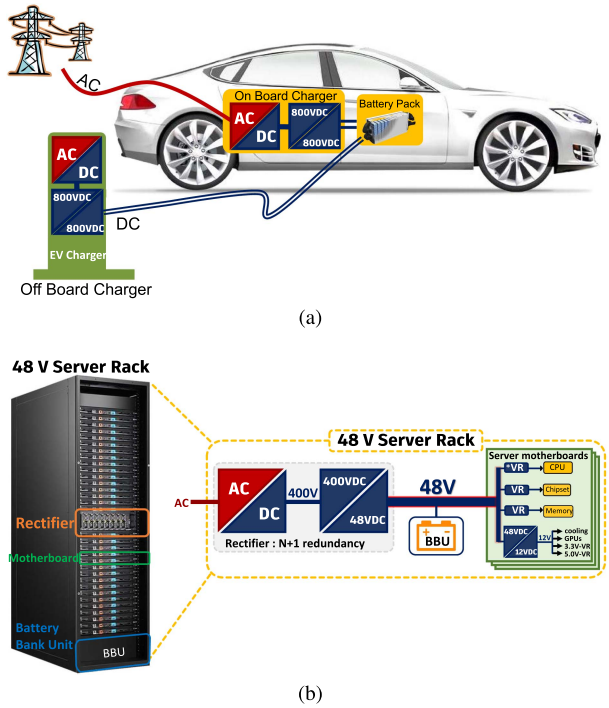

Fig. 1. Deployment of a high-voltage DC–DC resonant converter in (a) 800-V EV charging and (b) 48-V data center architecture.

3) They have parasitics with much improved reproducibility in large quantities.
4) PCB windings feature less leakage between transformer windings because of the flexibility of the winding interleaving and reduced number of turns.
5) There is better thermal management due to the increased surface-to-body ratio.
6) The design has a low profile and high power density.

However, it is not without its own limitations. Owing to the limitations on the number of layers for the PCB, the number of transformer turns is limited compared to Litz wire transformers. In some applications, such as 800-V EV chargers [6] or the 400-V LLC converter for the 48-V data center architecture [7], the voltage excitation per turn on the transformer winding is higher compared to its Litz wire counterparts, and the core cross-sectional area needs to be increased accordingly. The maximum flux density in the LLC transformer is calculated as follows:

$$B_m = \frac{V_o}{4n_s f A_e} \tag{1}$$

where n_s is the number of secondary series turns and A_e is the core cross-sectional area. In the 3-kW 400-to-48-V data center LLC converter, a four- or six-layer PCB board is preferred to reduce converter cost. A single-turn secondary is preferred to reduce conduction loss at an output current of 65 A. Thus, the single secondary turn is subject to the full output voltage (nominally equals 54 V). Fig. 2 shows an example of the 400-to-48-V LLC from [7] using matrix transformer and integrated magnetics. Each elemental transformer is subject to 54-V/turn excitation. That is 4.5 times higher voltage excitation than the legacy 12-V LLC converters [8]. This results in tens of times

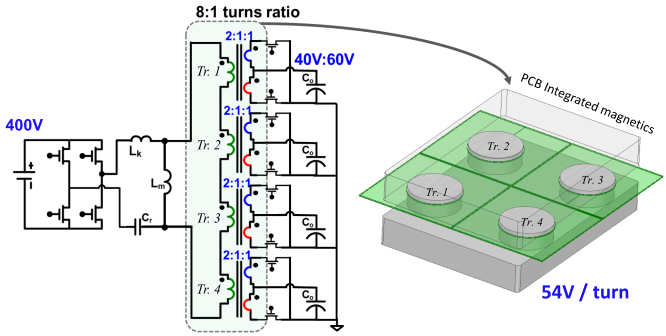

Fig. 2. Integrated magnetics of 1-MHz LLC for data centers [7].

the larger core size. With high operating frequency (megahertz range) and high volt-second, the large core design may exhibit dimensional effects that could degrade core performance [9]. The flux crowding, specifically in the custom-built planar magnetics, at the core sharp corners degrades the core loss. Solutions to such a problem were proposed by using arced corners [10]. However, such a solution is not applicable for the low-profile planar magnetics case [7], [11], [12], [13], [14]. Besides the flux crowding originating from core shape, the high-frequency ferrite core can suffer from flux nonuniformity due to dimensional resonance [15]. The phenomenon is mainly originating from the high dielectric constant of the ferrite material. This phenomenon has been a concern for specific applications working with a wide frequency spectrum, such as high-power wireless chargers [16] and electromagnetic interference filters [17]. The dimensional resonance is usually overlooked for low-frequency magnetics. However, as the interest increases toward high-frequency high-power magnetics [7], [18], the dimensional resonance becomes concerning for the mainstream power converter as well. The third and most pronounced concern is the eddy loss of the ferrite [19]. The conductivity of the ferrite material increases with frequency, jeopardizing the core loss for high-frequency converters [20]. The dependence of the eddy loss on the core cross-sectional area is discussed in [21], showing that high-power and large-core designs are more prone to increase eddy loss. A proper characterization of the ferrite dielectric constant and ac conductivity is essential for the proper evaluation of the core loss. The ferrite material characteristics can be measured by means of an impedance analyzer [22]. Measuring ferrite characteristics using the impedance analyzer is revisited in [23] with useful insights on the impact of sample dimensions, pressure, and temperature on the measured characteristics. In [24], a large-signal loss-based method is proposed to characterize the material ac conductivity. Such a method is contingent upon the accuracy of the core loss measurement technique [25], [26]. Unfortunately, there is a lack of characterization for the common low-loss MnZn ferrite materials widely used in high-frequency magnetics [5], [14], [27], [28], [29], [30], [31].

This article aims to evaluate the impact of high-frequency high-power converter design on magnetic core size and loss. This article presents an overview and characterization of dimensional effects on core loss and outlines a procedure for determining material characteristics such as conductivity and dielectric constant.

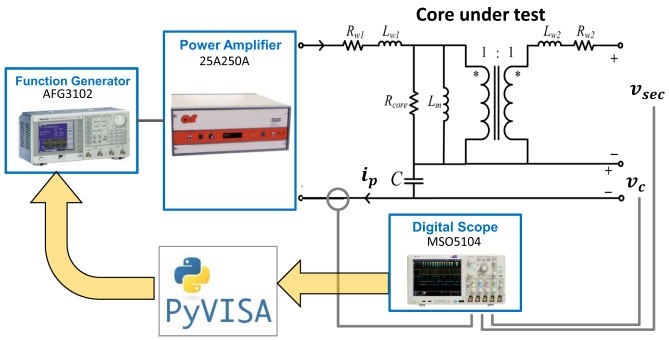

Fig. 3. Core loss test setup using the partial cancellation method [26].

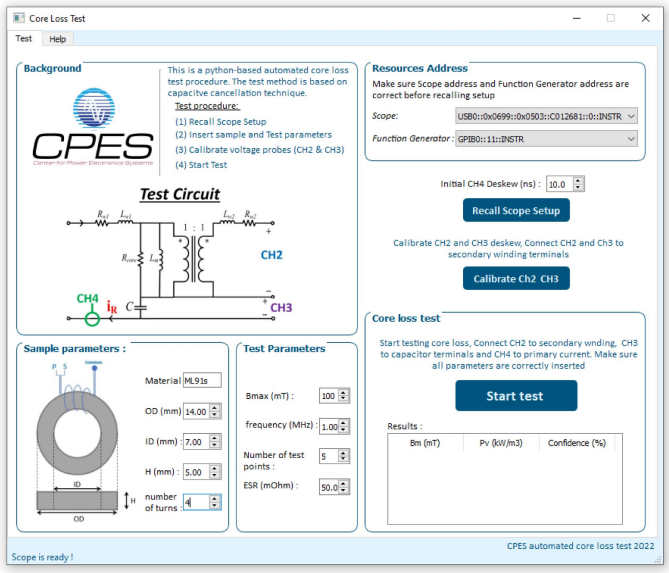

Fig. 4. Python-based automated core loss test program.

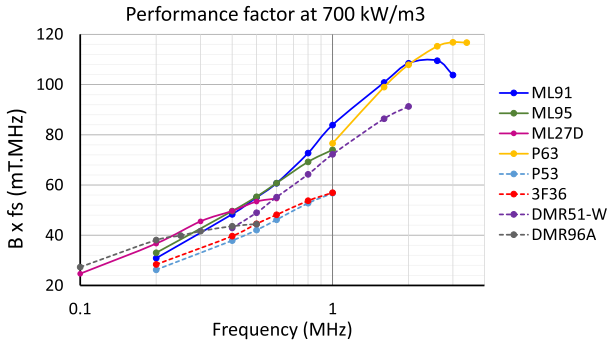

Fig. 5. Experimental evaluation of performance factor for different low-loss ferrite materials at a loss density of 700 kW/m^3.

Commonly used materials for high-frequency converters, such as ML91S, ML95S, ML27D, DMR51W, and P63, are analyzed, and their characteristics are provided to aid future designs. The authors also examine methods for evaluating dimensional effects and related loss through finite-element analysis (FEA). This article offers concise design guidelines for material selection and core shape to minimize these dimensional effects. The study concludes with a case study of a 1-MHz 3-kW LLC converter that demonstrates superior implementation, efficiency, and power density. The proposed converter achieved the highest power density of 700 W/in^3 and an efficiency of 98% in the 1-MHz converter class due to its careful design, which accounted for dimensional effects in the core loss. This article is an elaboration on a previously published conference paper [32], with more details on material characterization, FEA modeling, and model verification.

II. Problem Statement and Observations on Core Loss

The experimental core loss measurement is critical for the study presented in this article and is used throughout this article. The core loss is measured using the partial capacitive cancellation method [26]. This method can provide accurate core loss measurement at high frequency by eliminating the error originating from the phase discrepancy of the measuring probes. Fig. 3 shows the core loss test setup using the partial cancellation method. The core under test has two windings (primary and secondary), and a sinusoidal excitation is applied from the primary side. The excitation amplitude and frequency are tuned using a function generator. The primary current i_p, secondary voltage v_{sec}, and resonant capacitor voltage v_c are measured via a digital oscilloscope. The core loss can be extracted by integrating the voltage on the resonant link $(v_{\text{sec}} + v_c)$ and i_p over time. This method reduces the core loss error caused by the phase discrepancy between the voltage and current probes. It also uses a perturbation in the phase between the current and voltage probes to eliminate the phase discrepancy error in case the excitation frequency is different from the resonant frequency. A total of six electrical measurements are required to calculate one loss point at a given excitation. To simplify the test setup and obtain a consistent and fast measurement, a Python-based automated test program has been developed. Fig. 4 shows the graphical interface of the developed automated core loss test, which coordinates the function generator and the scope to automate the excitation and measurement process.

The survey of a variety of core materials is more manageable by using the automated core loss test platform. Multiple materials have been tested at a wide frequency range from 100 kHz to 3 MHz, and compared using the performance factor metric $(B_m \times f)$. The materials are tested using small toroid samples with dimensions OD $=$ 14 mm, ID $=$ 7 mm, and $H = 5$ mm. OD stands for outer diameter in millimeters, ID stands for inner diameter, and H stands for height. The materials are compared based on the performance factor $B_m \times f$, as shown in Fig. 5. According to Faraday's law, the product $B_m \times f$ is proportional to the excitation voltage V_{exc} and inversely proportional to the core cross-sectional area, i.e.,

$$\text{performance factor} : B_m \times f \propto \frac{V_{\text{exc}}}{A_e}. \tag{2}$$

It is desirable to have a high-performance factor, as a material with a higher performance factor can provide more power (higher V_{exc}) or can have a smaller size at the same level of loss. The performance factor of a given material will generally increase with frequency until it reaches a peak value, after which

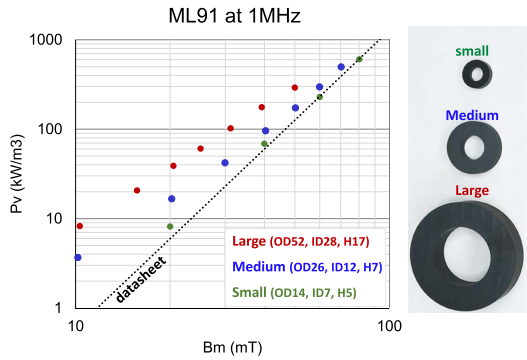

Fig. 6. Core loss density at 1 MHz for different core sizes of material ML91S.

there is no point in pushing the frequency further, and switching to a better material is recommended. The collective performance factor in Fig. 5 shows an uprising trend versus the excitation frequency, which implies that increasing the frequency helps with improving power density by reducing the core volume. Fig. 5 can be used to identify the optimal ferrite material for a given frequency by selecting the material with the highest performance factor at that frequency. In this study, we are focusing on the 1-MHz frequency. There are three candidates: ML91S, P63, and DMR51W, with ML91S presenting the best performance.

The core loss is usually calculated by integrating the core loss density P_v over the core volume. In practice, P_v is characterized for specific core material by measuring the core loss of a small toroid sample at different frequencies and ac flux densities. Then, curve fitting is done to get an empirical model of the core loss using the Steinmetz equation

$$P_v = C_m f^{\alpha} {B_m}^{\beta} \tag{3}$$

where C_m, α, and β are the Steinmetz coefficients. The Steinmetz equation describes P_v as a function in only excitation frequency and amplitude.

The underlying assumption of the abovementioned approach is based on empirical modeling of the loss density from measurement data acquired from a specific core sample. Then, the model is generalized and used for a plethora of shapes and applications. However, this approach is not adequate for high-frequency core material. It is found from experimental measurements on different toroid sizes that P_v increases with core size or core cross-sectional area A_e. Fig. 6 shows the core loss density for material ML91S measured for the three toroid samples at 1 MHz. Three toroid samples with different sizes were tested, and the dimensions are shown in the figure. The measured P_v for the small toroid (green) matches the datasheet Steinmetz model (black dashed line) from Table I. In contrast, the larger toroid samples show higher loss density than that in the datasheet. A similar test was carried out on the other two materials: DMR51W from DMEGC and P63 from ACME, as shown in Fig. 7. The same conclusion is drawn from the two sets of measurements; there is higher core loss density with a larger core size. The toroid core features uniform flux distribution, which is the reason why it is widely used to characterize material losses. The above test data are also measured on toroid samples yet with different sizes to study the impact of the size on the core loss density. Therefore, the loss discrepancy between the different toroid sizes and datasheet has little to do with the flux distribution uniformity.

TABLE I
DATASHEET STEINMETZ COEFFICIENTS*

Material	C_m	α	β
ML91S	6.49E-6	1.938	3.335
P63	1.25E-5	1.661	2.413
DMR51W	2.78E-5	1.755	2.903

*P_v in kW/m^3, f in Hz, and B_m in T.

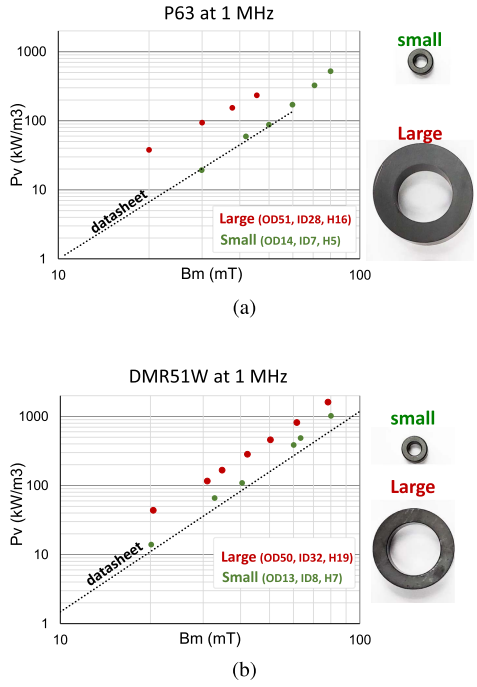

Fig. 7. Core loss density at 1 MHz for different core sizes of material: (a) P63 and (b) DMR51W.

The issue of core loss would be further complicated by using custom-made core shapes like the one in integrated magnetics (see Fig. 2), where the flux distribution will be less uniform. It would be interesting to see how much discrepancy exists between the tested core loss and the modeled core loss (using datasheet Steinmetz coefficients) in the integrated magnetics. Fig. 8 shows the comparison between the tested loss of the four-leg core from the 400-to-48-V LLC compared to the modeled loss using 3-D FEA (eddy simulation). The modeled FEA loss is calculated by feeding the software with the Steinmetz coefficient from Table I. The FEA model then calculates the core loss density at each mesh element using the Steinmetz equation. Then, the core loss density is integrated over the complete core volume. Therefore, the FEA model results shown in Fig. 8 reflect the datasheet parameters.

As seen from previous observations, the datasheet coefficients could result in misleading core loss estimation under various core sizes or shapes. That is not to say that the datasheet findings

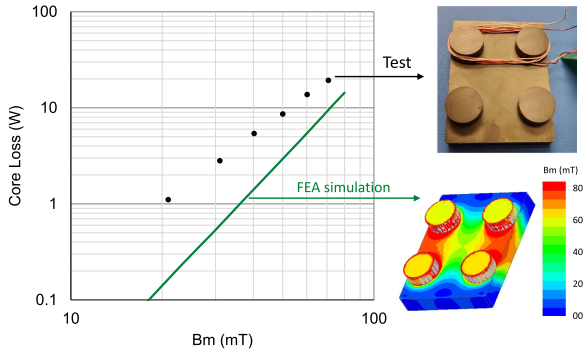

Fig. 8. Comparison between the tested (blue) and simulated (red) loss of the integrated core of matrix transformer with material ML91S at 1 MHz.

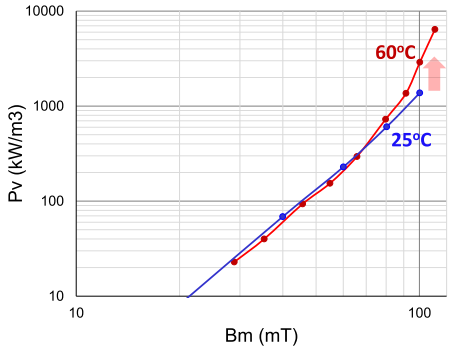

Fig. 10. Tested core loss density of ML91S material from Proterial at 25 °C and 60 °C.

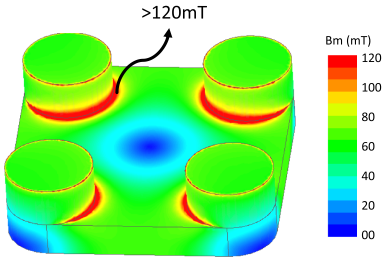

Fig. 9. Flux distribution in four-leg core for a planar transformer at 1 MHz designed at average $B_m = 60$ mT.

are not accurate. In fact, the measured losses of the small toroids in Figs. 6 and 7 agree with the datasheet model. However, the Steinmetz model itself is limited and does not factor in the core size/shape. One has to be careful when using the Steinmetz model to calculate core loss, particularly at high frequencies. This article is an attempt to study the dimensional effects on core loss in a high-power high-frequency transformer.

III. Dimensional Effect on Core Loss

Multiple factors related to the core dimensions, shape, or size can impact the core loss and cause discrepancies between the actual measured loss and the modeled loss. These dimensional factors or effects are summarized as follows.

A. Flux Crowding

Steinmetz coefficients are derived from the curve fitting of core loss measured from a specific ferrite sample. Usually, the ferrite sample is a toroid core with small dimensions (small A_e and small thickness) to guarantee uniform flux distribution. However, in reality, the core size and shape will depend on the application. In a PCB transformer, a low-profile small-window custom-made core shape is more convenient to use. In such a core, the flux is highly nonuniform, and there is flux crowding at the inner corners, as shown in Fig. 9, of the integrated core of four transformers. The crowding appears due to the high discrepancies in the reluctance of the flux paths within the planar magnetic core.

Some ferrite materials are categorized as "perminvar" materials [33], [34], which benefit from low hysteresis loss at low magnetic fields and high frequencies. However, strong magnetic fields or excessive mechanical stress can cause irreversible changes in permeability and loss characteristics of the material. Material ML91S falls under this category. Therefore, such material has limitations on the maximum flux density, and this limit is far lower than the saturation limit. This makes these high-frequency materials handle the flux crowding very poorly. To inspect the impact of flux crowding on core loss, P_v is measured at 25 °C and 60 °C for material ML91S at 1 MHz, as shown in Fig. 10. B_m is intentionally pushed beyond the recommended value by the supplier (50 mT) to observe the impact of flux crowding or high flux density on the core loss. P_v at 60 °C shows a rapid increase beyond 70 mT compared to the room temperature loss. Therefore, the Steinmetz equation or datasheet model, if wrongly used outside their intended B_m, f, and temperature ranges, will underestimate the core loss at higher working temperatures and higher B_m. This is the case at the corners of planar cores where high flux crowding is found. The flux crowding will cause localized loss and heat spots in the inner corners of the core.

B. Dimensional Resonance

The high-frequency ferrite material has a finite permittivity value, meaning that there is an induced electric field inside the ferrite material. The electric and magnetic field interaction tends to redistribute the magnetic field inside the ferrite core. The flux density distribution in an infinite straight core piece with thickness d is described according to [15] as follows:

$$B(x) = \mu H(x) = \mu H_o \frac{\cos(j\ k\ x)}{\cos(j\ k\ d/2)} \tag{4}$$

where H_o is the magnetic field at the surface of the core and k is the complex wavenumber. Equation (4) is derived from the Maxwell equations, solving the electric and magnetic fields inside a ferrite slap under sinusoidal excitation. It describes the spatial magnetic field $H(x)$ and flux density $B(x)$ distributions. The magnetic field follows a decaying sinusoidal distribution inside the ferrite core, and the sinusoidal peak is found at the center of the core ($x = 0$), as shown in Fig. 11. The magnetic field reduces at the boundary of the core ($x = d/2$), to what it would be at zero frequency (H_o). The wavenumber k is a function of the material characteristics μ and ϵ, which is

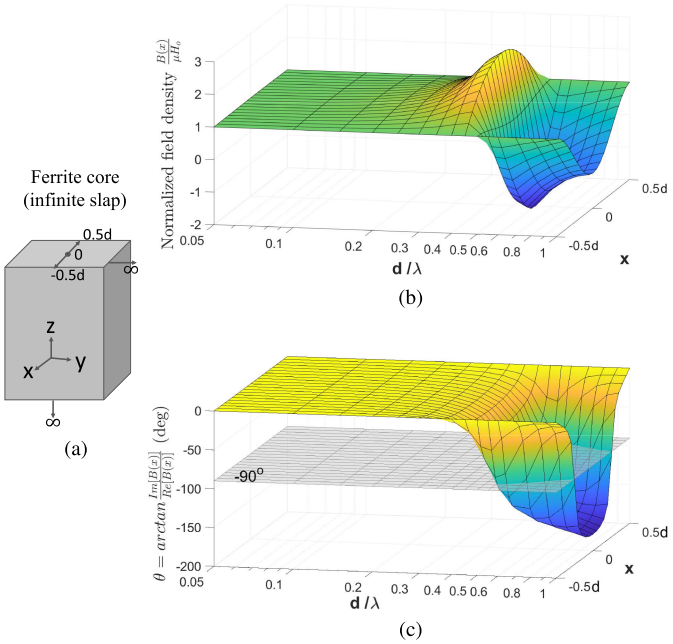

Fig. 11. Dimensional resonance in (a) ferrite core with thickness d, showing magnetic field distribution. (b) Real flux component. (c) Angle of the flux density vector $B(x)$.

defined as

$$k = k' - jk'' = \omega\sqrt{\mu\epsilon} \tag{5}$$

where ω is the angular excitation frequency, μ is the complex permeability, and ϵ is the complex permittivity, and are defined as

$$\mu = \mu' - j\mu'', \qquad \epsilon = \epsilon' - j\epsilon''_{\text{eff}} \tag{6}$$

where μ' is the real permeability of the material (slope of the B–H curve) and μ'' is the imaginary permeability and represents the magnetic loss (hysteresis loop loss of the B–H curve). ϵ' is the dielectric constant of the material, and ϵ''_{eff} is the effective imaginary permittivity, which represents the electric loss in the material. The real and imaginary wavenumber can be rewritten as

$$k' = \frac{\omega}{\sqrt{2}}\sqrt{|\mu||\epsilon| + (\mu'\epsilon' - \mu''\epsilon''_{\text{eff}})} \tag{7}$$

$$k'' = \frac{\omega}{\sqrt{2}}\sqrt{|\mu||\epsilon| - (\mu'\epsilon' - \mu''\epsilon''_{\text{eff}})}. \tag{8}$$

The decaying sinusoidal distribution has a wavelength λ of

$$\lambda = \frac{2\pi}{k'} = \frac{2\sqrt{2}\pi}{\omega\sqrt{|\mu||\epsilon| + (\mu'\epsilon' - \mu''\epsilon''_{\text{eff}})}}. \tag{9}$$

The effective imaginary permittivity ϵ''_{eff} can be described in terms of the dc conductivity of the material σ_{dc} and the intrinsic imaginary permittivity ϵ'' as

$$\epsilon''_{\text{eff}} = \epsilon'' + \frac{\sigma_{dc}}{\omega} \tag{10}$$

where σ_{dc} represents the dc loss in the material and ϵ'' represents the ac loss [16].

Fig. 11 shows the field distribution across the thickness (x-axis) of a ferrite core with thickness d according to (4). When the core thickness d is much lower than the wavelength λ, the field is uniformly distributed across the core. As d/λ increases, the field starts to concentrate in the middle of the core (forming a sinusoidal-like distribution). When d equals half of the wavelength ($d\lambda = 0.5$), the flux distribution takes the shape of a half-sinusoidal wave. When $d/\lambda > 0.5$, the magnetic field starts to flow out of phase within the core and causes circulating flux within the core. It is worth noting that the term d/λ represents both core thickness and frequency. This means that d/λ increases by increasing the core thickness at the same wavelength (or same frequency) or by increasing the frequency at the same core thickness.

The dimensional resonance is simulated using FEA by assigning the complex permeability and permittivity characteristics to the ferrite core material. Fig. 12 shows the field distribution on the round core leg of a UI core at different d/λ ratios. It can be seen that the core suffers from high flux crowding at the center when the core diameter d is approaching half the wavelength. As d exceeds half of the wavelength, the flux starts to circulate in the core, causing a drop in the average magnetic field density.

The dimensional resonance can be observed by measuring the core's apparent permeability. Fig. 13 shows the tested apparent permeability of a toroid from ML91S and the corresponding simulated flux distribution. As the frequency increases, the wavelength reduces, causing an increase in the flux and the apparent permeability. When half of the wavelength becomes smaller than the core thickness, the magnetic field starts to flow out of phase of the excitation current. This causes a drop in apparent core permeability and increased core loss, as shown in Fig. 13. The flux distribution in Fig. 13 shows the combined effects of (a) nonuniform distribution and (b) dimensional resonance. At 100 kHz, the flux is higher toward the inner radius. The same happens at 500 kHz. Starting from 1 MHz, the flux is observed to increase at the center, accompanied by an increase in the apparent permeability. Close to 3 MHz, half of the spatial dimensional resonance wavelength becomes smaller than core thickness, resulting in circulating flux in the core and collapse in the measured apparent permeability. As observed from Fig. 13, operating the core beyond the threshold ($d > 0.5\lambda$) is useless due to the circulating flux in the core and the collapse of apparent permeability. Even below the dimensional resonance threshold (1 MHz $< f <$ 2.5 MHz), the flux distribution is highly nonuniform and concentrated at the center, causing increased core loss.

Fig. 14 shows the tested permeability of the three toroid samples of material ML91S mentioned earlier in Fig. 6. It can be seen that dimensional resonance occurs at a lower frequency for the large core, where half of the wavelength meets the large core thickness at a lower frequency of 1.8 MHz. The tested material (ML91S) is recommended to run up to the 3-MHz range, but this is only for small core sizes whose thickness is still much smaller than $\lambda/2$ at 3 MHz. However, as the core size goes larger, the recommended operating range should be reduced. For example, the large toroid (red) operating range should be limited to 1 MHz or lower.

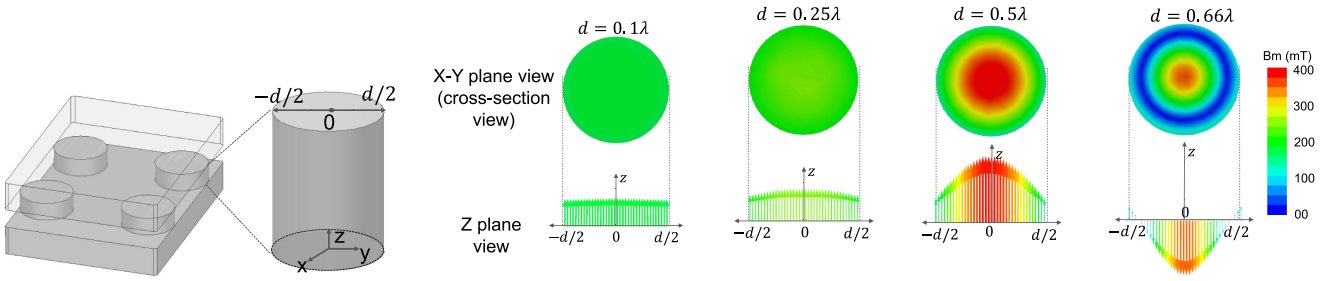

Fig. 12. Simulation of magnetic field density distribution in (a) integrated core with round leg at (b) $d/\lambda = 0.1$, (c) $d/\lambda = 0.25$, (d) $d/\lambda = 0.5$, and (e) $d/\lambda = 0.66$. The top picture shows the magnitude of the field density in the cross-sectional view, and the bottom picture shows the direction of the field (field vector) from the Z-plane view.

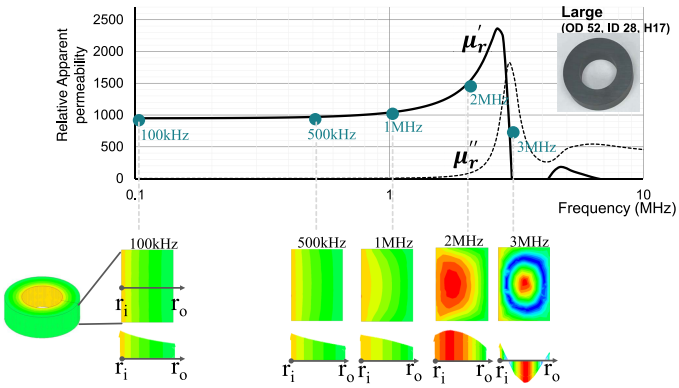

Fig. 13. Tested apparent permeability of a toroid from ML91S, and corresponding simulated flux distribution with permeability $\mu_r = 1000 - j35$ and permittivity $\epsilon_r = 30k - j6k$.

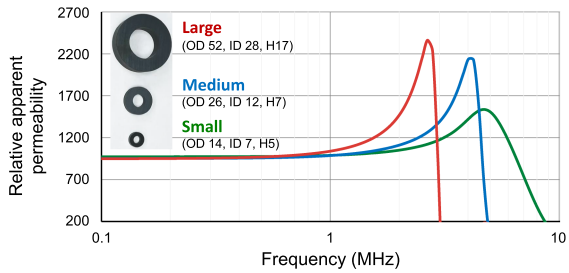

Fig. 14. Tested permeability of three toroid samples using material ML91S.

C. Eddy Core Loss and Skin Effect

The core loss is comprised of two main loss components: hysteresis loss and eddy loss. The weight of each loss component is dependent on the core material. The ferrite materials have a low electric conductivity, which reduces the eddy loss components and makes them good candidates at high frequencies >100 kHz. However, ferrite materials are basically semiconductors; therefore, the high rate of change of source flux induces ac currents to flow inside the core. These ac currents are responsible for the eddy core loss. Then, eddy flux is generated in the core to counteract the induced eddy currents. The induced eddy flux causes a skin effect in the core where the flux is concentrated on the core surface. The skin depth is defined as the distance from the core surface to where the flux density decreases to $1/e$ of the value at the core surface. The skin depth of the ferrite

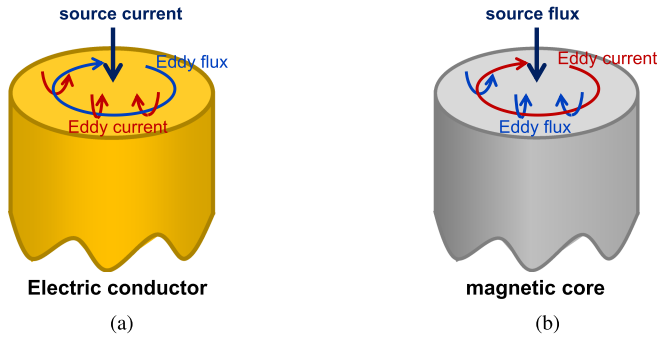

Fig. 15. Skin effect mechanism in (a) conductor and (b) magnetic core.

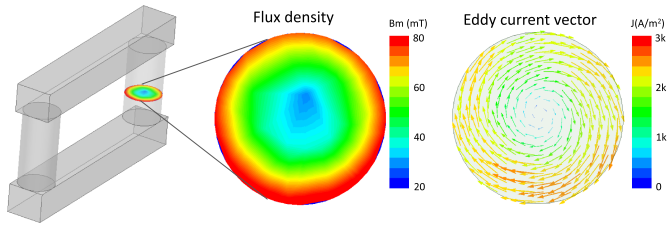

Fig. 16. FEA simulation of the skin effect in ferrite on the cylindrical core shape at 1 MHz, the conductivity of 0.9 S/m, and the core radius of 30 mm.

is calculated as a function of the imaginary wavenumber as follows [35]:

$$\delta = \frac{1}{k''} = \frac{1}{\mathrm{Im}[\omega\sqrt{\mu\epsilon}]}. \tag{11}$$

The skin depth can be represented as a function in the effective ferrite conductivity σ_{eff} as

$$\delta = \frac{1}{\mathrm{Im}\left[\omega\sqrt{\mu\left(\epsilon' - j\frac{\sigma_{\text{eff}}}{\omega}\right)}\right]} \tag{12}$$

where the effective ferrite conductivity can be calculated from the effective imaginary permittivity as

$$\sigma_{\text{eff}} = \omega\epsilon''_{\text{eff}}. \tag{13}$$

This mechanism of the eddy current and skin depth is analogous to the induced eddy currents causing skin effects in an electric conductor, as shown in Fig. 15. Fig. 16 shows FEA simulation for ferrite core with a conductivity of 0.9 S/m running at 1 MHz. The skin effect is apparent from the flux distribution (on the left).

The vectors of circulating eddy currents are also shown (on the right), which cause increased eddy core loss.

The eddy loss in the ferrite is usually assumed to be very small, and it is included in the Steinmetz model. The Steinmetz model is derived empirically from measured loss on a certain core sample and only characterizes the losses as functions in frequency and flux density. However, the eddy core loss is intrinsically dependent on the core cross-sectional area or the core thickness; similarly, the conductor eddy loss is dependent on the wire cross-sectional area. Such dependence on core dimensions is not accounted for in the Steinmetz model. The Steinmetz model only models dependence on flux density and frequency.

The core thickness needs to be smaller than the ferrite skin depth to avoid the skin effect. On the other hand, eddy loss is inevitable, and it is an intrinsic part of the core loss. According to the eddy loss density model listed in [21], the eddy loss density is characterized by a straight rounded or squared core shape with uniform flux as follows:

$$P_{v_{\text{eddy}}} = k_w \frac{\pi}{4} \sigma_{\text{eff}} A_e f^2 {B_m}^2 \tag{14}$$

where k_w is the waveform factor, $k_w = 1$ for sinusoidal excitation, and $k_w = 8/\pi^2$ for rectangular voltage excitation. σ_{eff} is the material effective conductivity and A_e is the core cross-sectional area. The eddy loss density is proportional to the material conductivity and core area. Also, eddy loss increases with f^2. The hysteresis loss, on the other hand, is only proportional to f, which indicates the dominance of eddy loss at high frequency. The classical eddy loss model in [19] shows that the eddy loss can be calculated for elongated core shape or laminated core as a function in the core thickness d as

$$P_{v_{\text{eddy}}} = k_w \frac{\pi^2}{6} \sigma_{\text{eff}} d^2 f^2 {B_m}^2. \tag{15}$$

Even though (14) and (15) are approximate models with some assumptions, they still introduce an intuition on how the eddy loss is impacted by the core A_e in round cores or thickness d in elongated and laminated cores. The large core design is prone to suffer from increased eddy loss density, which is added to the intrinsic hysteresis losses of the material. As the voltage excitation on the transformer winding increases, the core cross-sectional area of the core has to increase, as shown in (1). For a fixed frequency and flux density, the core area A_e is linearly proportional to the volt/turn on the transformer winding. Increasing the voltage rating on the power converter will result in an increase in the core loss density due to the larger core size design. Fig. 17 shows the simulated eddy loss of the four-leg integrated transformer core at 1 MHz and 60 mT. The details of the simulation methodology will be discussed in the next section. The volt/turn is swept from 6 to 100 V per turn. The impact of the increase of the transformer voltage on the core loss density can be seen. At 12 V/turn, which is the case of the legacy 400-to-12-V converter of the data center, the eddy loss is significantly smaller than the hysteresis loss. However, as the converter voltage increases to 48 V/turn (in the case of the 400-to-48-V converter), the eddy loss is significantly higher, even higher than the hysteresis loss, causing the total core loss density to almost double.

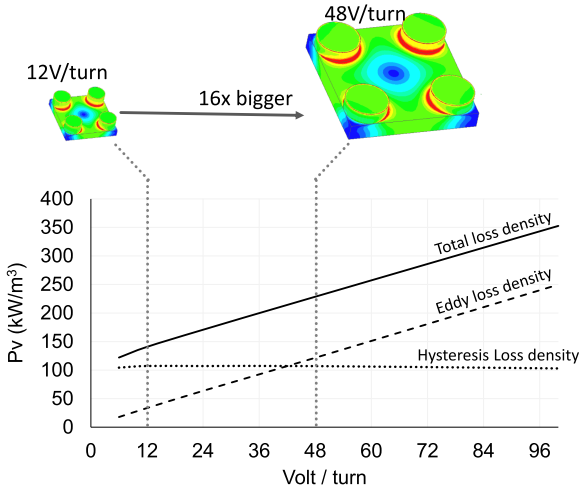

Fig. 17. Impact of volt/turn of the integrated planar magnetic core on the core loss density.

The Steinmetz model can account for frequency using the α coefficient, flux density using the β coefficient, and conductivity using the C_m coefficient. However, the Steinmetz model overlooks the cross-sectional area factor, so it cannot accurately predict the loss for any core size, as shown earlier in Figs. 6 and 7. Furthermore, the effective ferrite conductivity σ_{eff} is not a fixed value but is dependent on the frequency (increases with excitation frequency), as shown in (13). The dc conductivity σ_{dc} is usually included in the ferrite suppliers' datasheet, which is an underestimation of the effective (frequency-dependent) ferrite conductivity. The eddy loss depends on the total effective conductivity value σ_{eff}, which is not found in most ferrite datasheets.

IV. Measurement of Ferrite Characteristics and FEA Simulation of Dimensional Effects

Dimensional resonance and skin effect are highly dependent on the material complex permittivity ϵ and complex permeability μ, as discussed in (4)–(12). The eddy loss is also dependent on the effective ac conductivity, as discussed in (14) and (15). These characteristics are frequency dependent and need to be evaluated at the frequency of interest to estimate the core loss better. Moreover, the dimensional resonance model in (4) or the eddy loss model in (14) is approximated and derived based on 1-D or 2-D core shape assumptions. This makes them have low fidelity in the case of custom-made core shapes for integrated magnetics. An FEA is more appropriate and accurate in that case. In this section, the measurement of the ferrite characteristics is presented, followed by a detailed explanation of how to incorporate these characteristics in the FEA model to evaluate the dimensional effects and their related losses.

A. Measurement of Ferrite Characteristics

The real permeability and dc conductivity are often given in the ferrite datasheet; however, the remaining characteristics are rarely found. To obtain more accurate core loss for designing the high-frequency magnetics, the characteristics of a set of ferrite

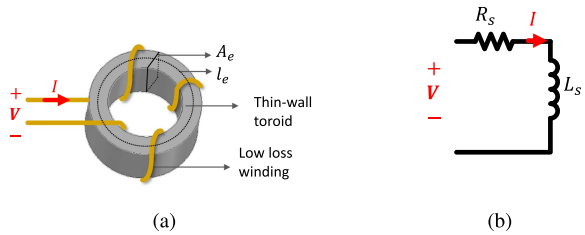

Fig. 18. Magnetic test sample. (a) Thin-walled toroid. (b) Equivalent circuit.

materials are measured and compared. There are two sets of measurements.

1) Complex Permeability Measurement: The permeability is measured by testing the impedance of a toroid sample from the desired ferrite material. For relatively low frequency (below the dimensional resonance), the equivalent circuit of the toroid wound inductor is represented by series R_sL_s network, as shown in Fig. 18. L_s represents the inductance due to the flux going through the core plus leakage flux. R_s represents the losses presented in the core and winding. The measured L_s and R_s relate to the real and imaginary permeability, respectively. L_s and R_s are measured using an impedance analyzer. Some considerations for proper measurement are as follows.

1) The winding's ac resistance and leakage inductance must be excluded from the measured R_s and L_s value. This can be done in two ways.

a) The resistance and the leakage inductance are measured separately using an air core toroid with the same size and number of turns as the ferrite sample. The measured inductance is the air core inductance, which is approximately regarded as the leakage inductance of the winding. The measured resistance and inductance are then subtracted from the measured resistance and inductance of the ferrite core inductor.

b) Compensation of leakage flux effect and winding resistance is accomplished by performing short-circuit compensation for the impedance analyzer using an air core inductor with the same number of turns. This will offset the impedance analyzer's measurements to exclude the winding's resistance and leakage.

2) A low turn number (here, four turns are used) distributed over the circumference of the toroid and far apart is preferred to reduce turn-to-turn capacitance. The parasitic capacitance between winding turns or between the winding and the core might impact and shifts the cutoff frequency (or resonance frequency) of the measured permeability.

3) A thin-walled toroid is preferred to avoid any excess loss from the eddy loss and avoids dimensional resonance at the frequency range of interest. Also, a thin toroid with a low outer/inner radius ratio ensures uniform flux distribution in the toroid.

The toroid impedance is measured using a Keysight E4990A impedance analyzer and a 16047 fixture, as shown in Fig. 19. The impedance analyzer is set to series L_sR_s measurement mode. The measured impedance of the toroid under test can then be

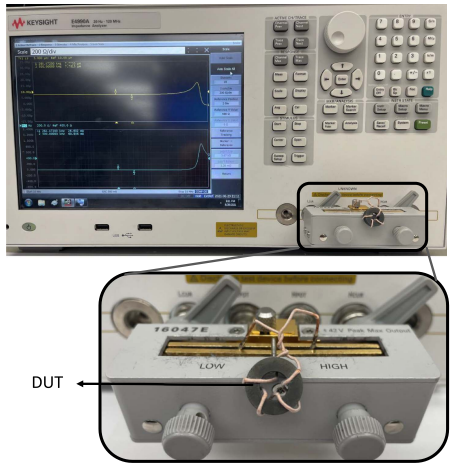

Fig. 19. Test setup for permeability measurement.

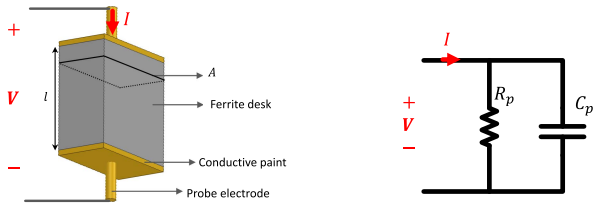

Fig. 20. Electric test sample. (a) Ferrite disk. (b) Equivalent circuit.

described as follows:

$$Z = R_s + j\omega L_s = j\omega(\mu' - j\mu'')\frac{n^2 A_e}{l_e} \tag{16}$$

where n is the number of turns and l_e is the toroid mean length. From (16), the complex permeability can be calculated as

$$\mu' = \mu_o \mu_r' = L_s \frac{l_e}{n^2 A_e} \tag{17}$$

$$\mu'' = \mu_o \mu_r'' = R_s \frac{l_e}{\omega\, n^2 A_e} \tag{18}$$

where μ_r' and μ_r'' are the relative real and imaginary permeability, respectively.

2) Complex Permittivity and Conductivity Measurement: The permittivity is measured by measuring the admittance of a ferrite desk. The measurement uses a parallel plate capacitive model, as shown in Fig. 20(a). The equivalent circuit is represented as capacitance C_p to represent the dielectric properties of the ferrite and R_p to represent the electric loss of the ferrite. Some considerations for proper measurements are also listed.

1) A thin electrode/plate area is preferred to avoid errors originating from the dimensional resonance. The dimensions of the cross-sectional area should be much smaller than the wavelength at the intended frequency [23].

2) Long sample (long distance between the two electrodes) ensures a uniform electric field in the tested sample and reduces the fringing of the electric field between the two electrodes. Here, a 4 mm × 4 mm × 2 mm desk sample is

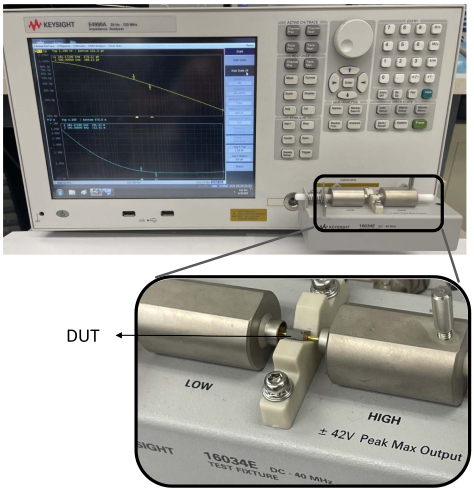

Fig. 21. Test setup for permittivity measurement.

used, and the electrode surface is placed on two adjacent 4×2 surfaces.

3) There should be zero air gap between the conductive electrode/plate and the ferrite surface. This is very difficult to achieve, no matter how flat the electrode plate is or how hard the pressure is between the electrode plate and the ferrite surface. This is due to the porous nature of the ferrite surface, causing micro air gaps between the electrode and the ferrite. To avoid such a problem, the ferrite surface on the two electrode sides is coated with highly conductive material (silver-coated copper conductive spray coating). This helps to achieve a perfect and uniform contact between the electrode and ferrite surface.

A 16034E fixture probe is used, as shown in Fig. 21. The impedance analyzer is set to parallel C_pR_p measurement mode. The measured admittance is expressed as follows:

$$Y = \frac{1}{R_p} + j\omega C_p = j\omega\left(\epsilon' - j\epsilon''_{\text{eff}}\right)\frac{A}{l} \tag{19}$$

where A is the ferrite surface area facing the electrode and l is the distance between the two electrodes. The complex permittivity is then calculated as a function of C_p and R_p as

$$\epsilon' = \epsilon_o\epsilon'_r = C_p\frac{l}{A} \tag{20}$$

$$\epsilon''_{\text{eff}} = \epsilon_o\epsilon''_{r_{\text{eff}}} = \frac{1}{R_p}\frac{l}{\omega\, A} \tag{21}$$

where ϵ'_r is the relative real permittivity and $\epsilon''_{r_{\text{eff}}}$ is the effective imaginary permittivity. Note that ϵ''_{eff} represents the total electric loss in the material (both dc and ac loss). The effective conductivity σ_{eff} can then be calculated according to (13). The dc conductivity and imaginary ac permittivity can be calculated independently from (10). The dc conductivity is simply the conductivity of the material measured at 0 Hz. Subtracting the dc conductivity from the effective conductivity yields the imaginary permittivity ϵ''. Fig. 22 shows the breakdown of the measured effective conductivity into dc conductivity and imaginary (ac) permittivity of the material.

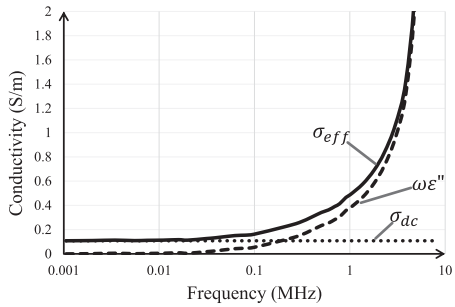

Fig. 22. Measured effective conductivity of ML91S and the breakdown into dc conductivity and imaginary permittivity.

The complex permeability, permittivity, and conductivity characteristics are measured for different low-loss MnZn ferrite materials ML91S, ML95S, ML27D, P63, and DMR51W. The measured materials are of great interest and widely used for the magnetic design [5], [14], [27], [28], [29], [30], [31] and cover a wide range of frequencies from 200 kHz to 3 MHz. The measured characteristics are listed in Fig. 23 for the reader's convenience. Material ML91S presented the least conductivity value and, hence, was chosen later for the 1-MHz design.

B. FEA Simulation of Dimensional Effects

Practically, there are some cases when one of the loss mechanisms is significantly larger than the others, and it is important to be able to differentiate between all the loss components and model them separately in the solver. For example, a small core may be dominated by hysteresis loss, while a larger core of the same material may have significant eddy loss at the same frequency. In order to separate the hysteresis loss from the eddy loss. Four components can represent the ferrite loss in FEA simulation: *core loss, magnetic loss, ohmic loss*, and *dielectric loss*. The FEA loss components are referred to in *italic* to differentiate them from the physical core loss components. These FEA loss components are described as follows:

$$\begin{aligned} P_{v-\text{FEA}}\ (\text{W/m}^3) = {} & \frac{1}{2\sigma}J.J^* \Rightarrow \text{ohmic loss} \\ & + \frac{\omega\epsilon''}{2}E.E^* \Rightarrow \text{ dielectric loss} \\ & + \frac{\omega\mu''}{2}H.H^* \Rightarrow \text{hysteresis loss} \\ & + C_m f^x B_m^y \Rightarrow \text{core loss} \end{aligned} \tag{22}$$

where J is the current density, E is the electric field, and H is the magnetic field. The superscript $*$ denotes the conjugate value. C_m, x, and y are the Steinmetz coefficients fed to FEA. The total core loss is then calculated by integrating the loss density $P_{v-\text{FEA}}$ over the volume of the core as follows:

$$P_{\text{FEA}}\ (W) = \int_{V_{\text{core}}} P_{v-\text{FEA}}\ dv. \tag{23}$$

Equation (23) can account for the nonuniform distribution of the flux due to flux crowding, dimensional resonance, or skin effect since it calculates the loss density for every mesh element in the

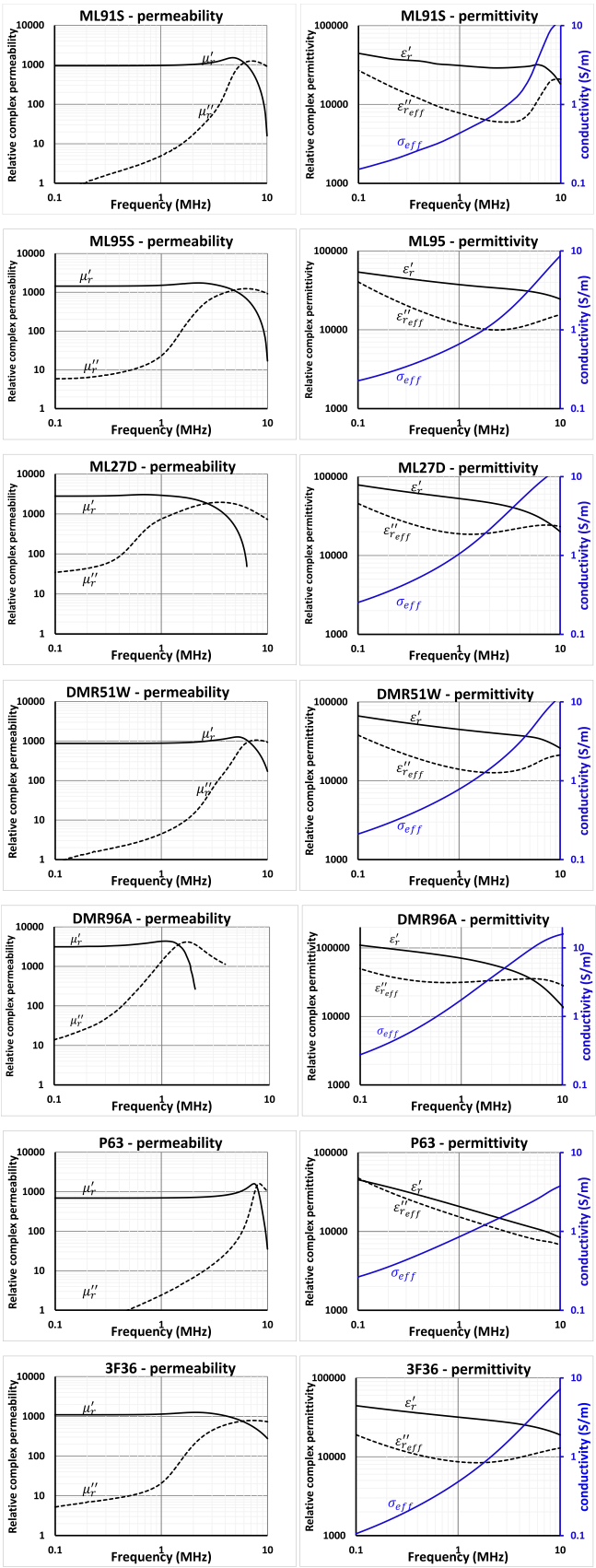

Fig. 23. Measured characteristics for different low-loss MnZn ferrite materials.

core and then integrates the losses in all the mesh elements in the core volume. Some loss components in (22) may be redundant. This redundancy offers multiple approaches to identify various core loss mechanisms. Therefore, comprehending each loss component, its representation, and its limitations is crucial for conducting a comprehensive core loss assessment.

1) *Ohmic loss:* It represents the conduction loss in the ferrite, and it is related to the material conductivity. If the dc conductivity is used, then the *ohmic loss* will represent the part of eddy loss related to the ferrite dc resistance only. If effective conductivity σ_{eff} is used, then the *ohmic loss* will represent the whole eddy loss.
2) *Dielectric loss:* The *dielectric loss* is calculated from the imaginary permittivity. The FEA simulation calculates the *dielectric loss* using the dielectric loss tangent $\tan\delta_e = \epsilon''/\epsilon'$. In the FEA, if the ac imaginary permittivity ϵ'' is used, then the *dielectric loss* will represent only the ac-related eddy loss due to displacement current. If the effective ϵ''_{eff} is used, then the *dielectric loss* will represent the total eddy loss.
3) *Hysteresis loss:* It represents the hysteresis loss of the ferrite and is calculated using the magnetic loss tangent $\tan\delta_m = \mu''/\mu'$. In order to exclude the dimensional effects and eddy loss from the μ'', μ'' should be measured on a core sample where the hysteresis loss dominates and the eddy loss is negligible; this is satisfied on small toroid samples with a thin wall.
4) *Core loss:* As referred to in the FEA simulation, it is calculated using a P_v–B_m relation in the simulation software. For the ferrite material, the Steinmetz equation is widely used. The Steinmetz loss, as mentioned before, lumps all the loss components together in an empirical model (hysteresis loss and eddy loss). The loss calculated from the Steinmetz model is called *core loss* in Ansys FEA simulation. If the Steinmetz model is derived from a sample where the hysteresis loss is dominating (small toroid with a thin wall), the *core loss* can be used to represent the hysteresis loss. On the other hand, if the Steinmetz model is derived from a large core sample where the eddy loss is significant, the core loss will represent the total loss in that sample (hysteresis + eddy). However, the latter case is not a proper way of material characterization because there is no way to differentiate between the hysteresis loss and eddy loss. This model would be only good for that specific core sample (the large sample).

There are three methods available for calculating the eddy loss, all of which result in identical eddy loss and magnetic/electric behavior in the core. These methods offer designers flexibility in choosing the most suitable approach based on readily available characteristics.

1) *Method 1:* Using the dc conductivity σ_{dc} and the imaginary permittivity ϵ'', the eddy loss will be the sum of the *ohmic loss* and *dielectric loss*.
2) *Method 2:* Using the effective conductivity σ_{eff} and setting the dielectric loss tangent $\tan\delta_e = 0$, the eddy loss will be represented by the *ohmic loss* only.

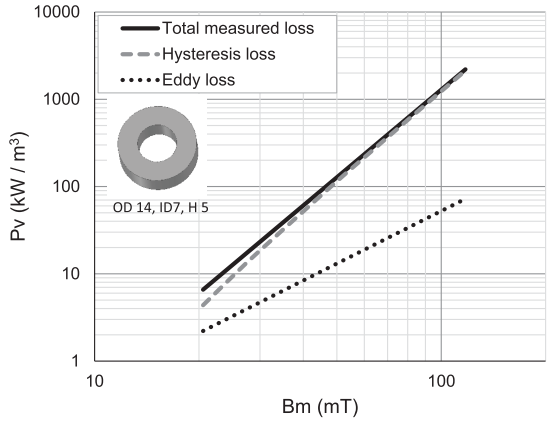

Fig. 24. Measured loss on thin-wall toroid at 1 MHz, and the breakdown of hysteresis loss and eddy loss.

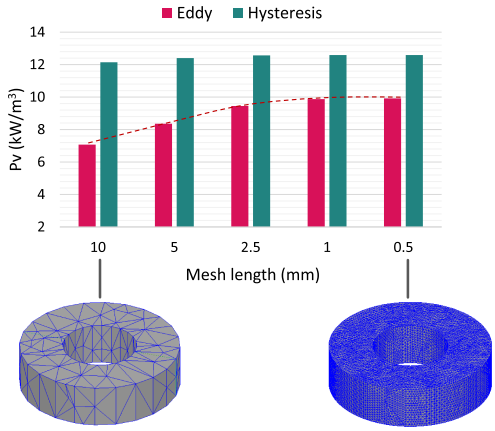

Fig. 25. Impact on initial mesh length setting on the FEA eddy loss accuracy.

3) *Method 3:* Using the effective loss tangent $\tan\delta_e = \epsilon''_{\text{eff}}/\epsilon'$ and setting $\sigma = 0$, the eddy loss will be represented by the *dielectric loss* only.

The three methods are illustrated in the following equation:

$$\begin{aligned} P_{v-\text{eddy}} &= \frac{1}{2\sigma_{\text{dc}}} J.J^* + \frac{\omega\epsilon''}{2} E.E^* \Rightarrow \text{method 1} \\ &= \frac{1}{2\sigma_{\text{eff}}} J.J^* \Rightarrow \text{method 2} \\ &= \frac{\omega\epsilon''_{\text{eff}}}{2} E.E^* \Rightarrow \text{method 3.} \end{aligned} \tag{24}$$

If both the effective conductivity and effective imaginary permittivity are used, then the *ohmic loss* and *dielectric loss* become redundant and equal, and only one of them is used to represent the eddy loss. All the aforementioned three methods render the exact same loss. Note that the conductivity threshold between the conductor and the insulator in the FEA software should be set lower than the ferrite conductivity in order for the FEA to simulate the *ohmic loss* in the core. Also, the eddy effect and displacement current should be enabled for the core in order to calculate the *ohmic loss* and/or the *dielectric loss* in the core.

On the other hand, the hysteresis loss can be calculated using *core loss* or *hysteresis loss* if μ'' or the Steinmetz model is measured from the same core sample. However, there is a limitation to using the *hysteresis loss*. μ'' is measured using a small-signal measurement with an impedance analyzer, so it does not give a good representation of the actual large-signal loss of the hysteresis loop. Therefore, the Steinmetz model is used instead to calculate the hysteresis loss in the FEA simulation. The core loss is first measured in a core sample where the eddy loss is inherently small (thin-wall small toroid), as shown in Fig. 24. The hysteresis loss dominates the measured total loss (solid line). For better accuracy, the simulated eddy loss (dotted line) should be subtracted from the measured loss on the same sample to extract the pure hysteresis loss (dashed line). Then, this pure hysteresis loss is modeled in new Steinmetz coefficients and fed to the FEA simulation to calculate the *core loss*.

The mesh setting of the FEA simulation is important in calculating the core loss, more specifically, the eddy loss. In this article, the eddy solver is used, which simulates ac sinusoidal excitation only. The eddy solver has the ability of adaptive iterative meshing to refine the mesh automatically until a certain error threshold is met. However, it was found that the initial mesh setting of the core has a high impact on the accuracy of the eddy loss. An exercise is performed on the FEA simulation of a toroid core (OD26, ID12, H7), where the initial mesh length is controlled, and the eddy loss and hysteresis loss are observed. Fig. 25 shows the FEA simulated loss of a toroid core versus the initial mesh length setting. Setting a large initial mesh length or skipping the mesh setting of the simulated core results in around 30% deficit in the simulated eddy loss. The mesh setting also seems to have a less pronounced impact on the hysteresis loss. That is understood since a fine mesh is important to simulate the ac eddy currents in the core, which is the essence of the eddy loss. The eddy loss seems to converge at or below 1-mm mesh length. In the simulated case, for material ML91 at 1 MHz, 1 mm represents 2% of the skin depth. A rule of thumb can be deduced here that the initial mesh length setting should be 2% the skin depth or smaller.

The discrepancy between the core loss density P_v of different toroid sizes, which was reported earlier in Section II in Fig. 6, can be explained and verified in the light of the simulated dimensional effects. By measuring the material characteristics and feeding it to the FEA simulation, the simulated loss can account for the dimensional effects and eddy loss in the core. Fig. 26 shows the measured and simulated core loss of material ML91S at different toroid sizes. There is good agreement between the measured loss and the simulated loss after accounting for dimensional effects. Also, Fig. 27 shows the measured and simulated loss for the integrated four-leg core. The dimensional effects explain the discrepancy earlier found in Fig. 8. Fig. 27 shows agreement between the measured loss and the new simulated loss after accounting for dimensional effects.

V. Guidelines and Recommendations for Reducing the Dimensional Effects on Core Loss

In light of the previous discussion on the dimensional effects, we can draw a few rules to help mitigate their adverse implications on core loss. The dimensional resonance can be avoided

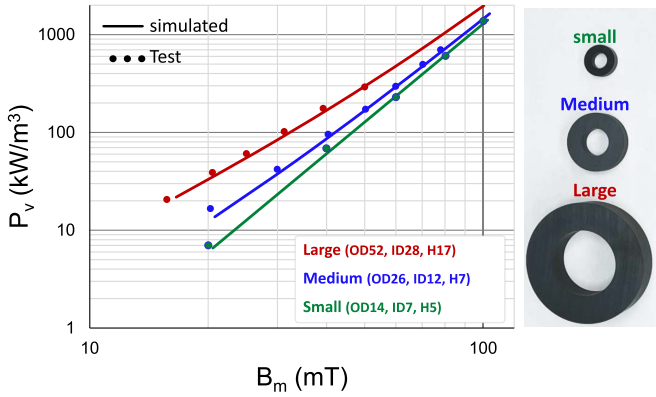

Fig. 26. Core loss comparison between simulation and measurements for material ML91S at different toroid sizes.

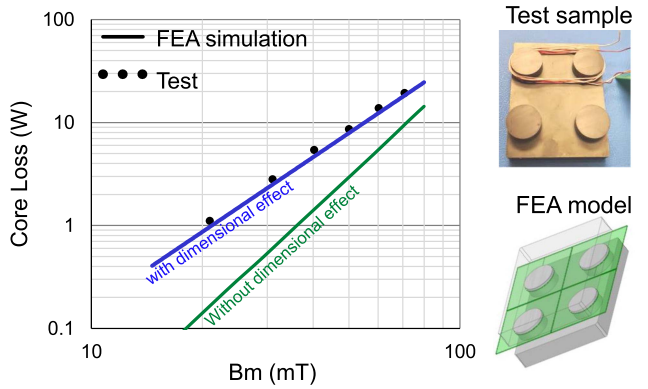

Fig. 27. Core loss comparison between simulation and measurements for integrated planar transformer core ML91S.

by ensuring that the core thickness or core diameter (in the case of a round-shape core) at the maximum operating frequency is smaller than half the wavelength in (9). However, at half of the wavelength, the flux distribution is still highly nonuniform, as shown in Fig. 12(d), and the apparent permeability of the core is at its peak point, as shown in Fig. 13. Therefore, it is recommended to operate the core in the flat permeability region far from the dimensional resonance peaks. A simple suggestion is to make the core thickness less than a quarter of the wavelength. The dimensional resonance limit can then be defined as

$$\text{dimensional resonance limit: } d \leq \frac{\lambda}{4} = \text{Re}\left[\frac{\pi}{2\omega\sqrt{\mu\epsilon}}\right] \quad (25)$$

where d is the core thickness. The imaginary parts of the permeability and permittivity have no impact on determining the wavelength, but only the distribution of the flux. Therefore, (25) can be simplified to

$$\text{dimensional resonance limit: } d \leq \frac{\pi}{2\omega\sqrt{\mu'\epsilon'}}. \quad (26)$$

Moreover, the skin effect causes flux crowding on the surface of the core and gradually decreases towards the center, as shown in Fig. 16. The core thickness should be smaller than the ferrite skin depth to avoid the skin effect. This makes the design limit

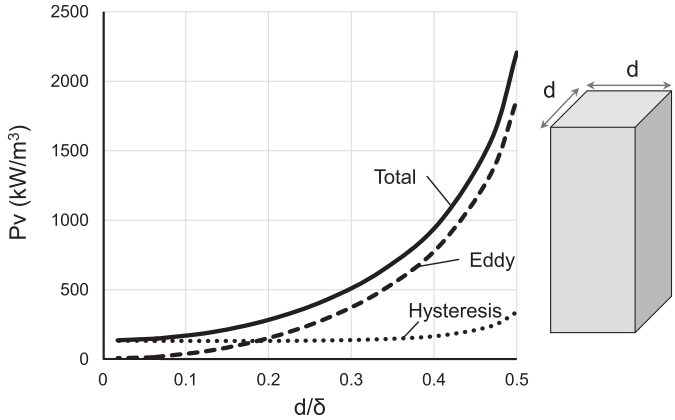

Fig. 28. Impact of core thickness on the eddy loss density (calculated for ML91S at 1 MHz and 50 mT).

to avoid skin effects as follows:

$$\text{skin effect limit: } d \leq \delta = \frac{1}{\text{Im}[\omega\sqrt{\mu\epsilon}]}. \quad (27)$$

The ratio between imaginary and real permeability μ''/μ' is very small in the ferrite materials. By neglecting μ'', (27) can be approximated as

$$\text{skin effect limit: } d \leq \frac{\sqrt{2}}{\omega\sqrt{\mu'\left(\sqrt{\epsilon'^2 + (\sigma_{\text{eff}}/\omega)^2} - \epsilon'\right)}}. \quad (28)$$

Equations (26) and (28) provide the design guidelines to avoid highly nonuniform flux distribution due to dimensional resonance and skin effect. Nevertheless, there is a more imminent challenge, which is the eddy loss. A significant eddy loss can appear in the core far before the skin effect, or dimensional resonance appear. The solution to eddy loss in the ferrite core is analogous to the solution of eddy loss in electrical conductors. The eddy loss can be reduced by reducing the effective area at which the eddy currents are circulating. According to (14) and (15), the eddy loss is proportional to the core area A_e or thickness squared d^2. To draw a conclusion on the appropriate size of the core to mitigate the eddy loss, we first study the impact of the core thickness on eddy loss density. Fig. 28 shows the simulated loss density on a core with thickness d. The x-axis shows the normalized core thickness over the material skin depth d/δ to account for the frequency and conductivity variations. We can see that at half the skin depth, the eddy loss dominates the total loss density in the core. The total loss density at 50% skin depth increased 15× compared to the value measured at 10% skin depth. We also notice that the hysteresis loss increases when the core thickness approaches half the skin depth as the core starts to experience severe flux crowding due to dimensional resonance. This proves that the eddy loss has a more pronounced and imminent impact on the core loss than the dimensional resonance or the skin effect for the ferrite materials. In order to avoid a severe increase in eddy loss, the core thickness should be kept below 10–20% of the skin depth. We can draw a new

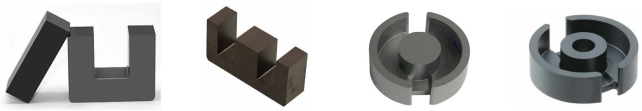

(a) (b) (c) (d)

Fig. 29. Off-the-shelf core shapes. (a) UI core. (b) EI core. (c) Pot core. (d) Pot core with hollow leg.

guideline for the eddy loss as follows:

$$\text{eddy loss limit: } d \leq \frac{1}{5}\frac{\sqrt{2}}{\omega\sqrt{\mu'\left(\sqrt{\epsilon'^2+(\sigma_{\text{eff}}/\omega)^2}-\epsilon'\right)}}. \quad (29)$$

Equation (29) states that the core thickness should be less than $1/5$ the skin depth to restrain the eddy loss in the core. However, the thinner the core, the lower the eddy loss. Similar behavior or trend is expected of the eddy and hysteresis losses versus d/δ in other ferrite materials since the x-axis is normalized over the skin depth, which accounts for the frequency and conductivity information. Therefore, it is safe to claim that the trend and conclusions from Fig. 28 can be generalized for different materials with different conductivities and for different frequencies as well. However, the exact ratio between the hysteresis and eddy losses could vary for different materials since different materials have different B_m and f exponents for the hysteresis loss and different conductivity as well.

VI. High-Frequency Matrix Transformer Design

The core shape can significantly impact the eddy loss density and, consequently, the core loss. For example, in a case of a single transformer or inductor core, Fig. 29 shows different off-the-shelf core shape options. In the UI core [see Fig. 29(a)], the flux is generated from the winding on one leg and returns through another leg with the same A_e and thickness as the winding leg. In the EI core [see Fig. 29(b)], the flux returning path is distributed on the two side legs, which are designed with half the thickness (half A_e) of the center leg. Therefore, the EI core will have less eddy loss density due to the plate and side legs' smaller thickness than the UI core. The pot core [see Fig. 29(c)] provides better space utilization as the side legs cover more perimeter, making the side leg and plate thickness even smaller than the EI core and, hence, smaller eddy loss. Even though the EI core and the pot core provide small eddy loss in the plate and the side leg, the center leg still suffers high eddy loss density. A pot core with a hollow center leg [see Fig. 29(d)] solves this problem by creating a hole in the center leg. This makes the effective thickness of the center leg smaller and reduces the eddy loss density. This makes the pot core with a hollow center leg a good solution for high-frequency designs. In order to test these intuitive conclusions, the core shapes in Fig. 29 are evaluated using FEA analysis, as shown in Fig. 30. The four core shapes are redesigned in the FEA platform to have the same effective cross-sectional area for a fair comparison. The losses compare at the same operating conditions (1 MHz, 50 mT), core cross-sectional area, and window size (same winding width). We can see from Fig. 30 that the pot core with a hollow leg gives the least core loss, mainly due to the reduced eddy loss. We also see that the EI core performs significantly better than the UI core because of the reduced eddy loss in the thinner plate and side legs. The hysteresis loss also reduces in the EI core and further in the pot core due to the reduced flux crowding discussed in Section III-A.

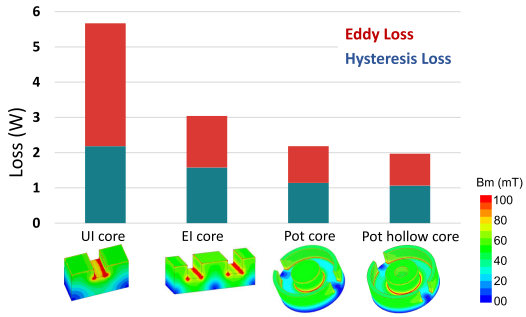

Fig. 30. Comparison between different off-the-shelf core shapes at 1 MHz and 50 mT.

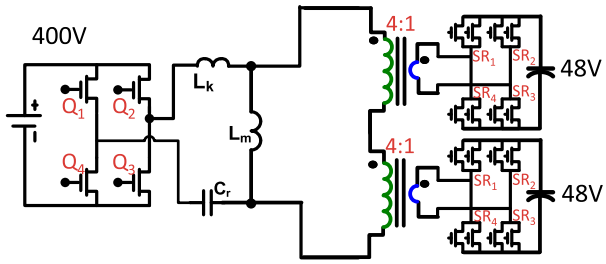

Fig. 31. Circuit diagram of 3-kW 400-to-48-V LLC with a matrix of two transformers.

The previous discussion gives some insights on reducing eddy loss in a single transformer or inductor core using the existing off-the-shelf designs. However, the case differs for an integrated planar core for a matrix of transformers. Here, for example, we present a case study of a 1-MHz 3-kW LLC converter for data centers' 48-V bus architecture. We study the case of an integrated matrix of two transformers for the LLC converter, as shown in Fig. 31. The two transformers can be implemented using two separate EI cores. However, integrating the elemental transformers into one core has the benefit of easier assembly, lower component count, and less footprint. The two EI cores of the two elemental transformers are integrated into a single UI core following the concept of flux cancellation [36], as shown in Fig. 32. However, after the integration into the UI core, it is found that the UI core has more loss than the two EI cores combined, as shown in Fig. 32(b) and (c). The plate thickness in the UI core is double the plate thickness of the EI core, hence higher eddy loss, specifically in the plate.

Some solutions to reduce eddy loss in integrated two transformers on a UI core are explored as follows.

1) *Hollow core:* The idea is to make the core's effective thickness smaller, helping to reduce the eddy loss, as shown in Fig. 33(b). The hollow core shows reduced eddy loss, as shown in Fig. 33(e).

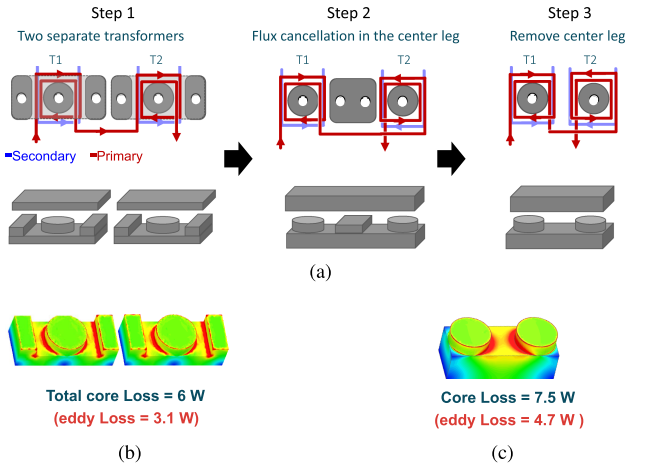

Fig. 32. Integration of two transformers. (a) Integration steps [36]. Corresponding core loss at 60 mT for (b) separate core solution and (c) integrated UI core solution.

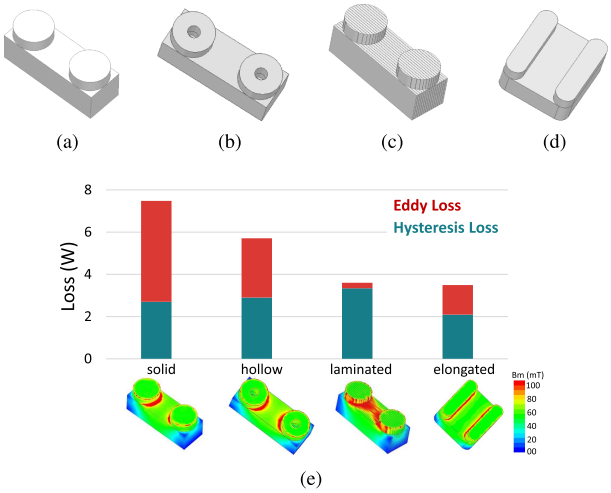

Fig. 33. Evaluation of different solutions for eddy core loss reduction in (a) solid round UI core using (b) hollow core, (c) laminated core, and (d) elongated core. (e) Loss comparison at 1 MHz and 60 mT with ML91S.

2) *Laminated core:* This solution is used to limit eddy loss in the steel core, as shown in Fig. 33(c). The eddy loss almost vanished, but the hysteresis loss increased for uneven flux distribution between laminates. Since the laminates have different shapes and reluctance, some laminates with high reluctance are underutilized. Others with low reluctance are crowded, resulting in nonuniform flux distribution and higher hysteresis loss. Nonetheless, solutions 1 and 2 are not practical to fabricate and assemble.
3) *Elongated core:* Elongating the core reduces the effective thickness, as shown in Fig. 33(d). This solution is similar to the solution of reducing eddy loss in solid copper wires by using thin PCB winding. One can see that it reduces the eddy loss without sacrificing flux distribution.

Solution 3 offers easier fabrication and assembly than solutions 1 and 2, and hence, it is used here. Reducing the core thickness reduces the eddy loss; the thinner, the lower the core loss. However, elongating the core eventually increases the winding

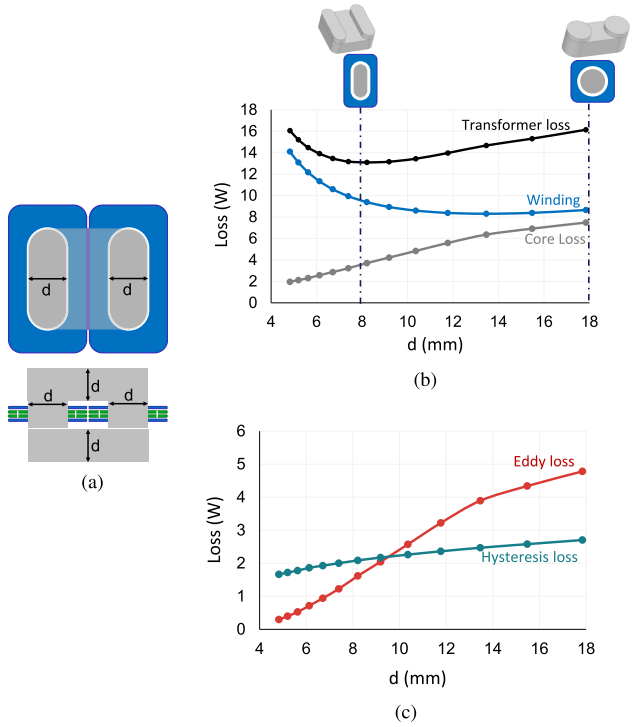

Fig. 34. Optimization of core thickness at same footprint, A_e, and B_m to reduce eddy loss. (a) Core shape. (b) Transformer loss. (c) Core loss breakdown.

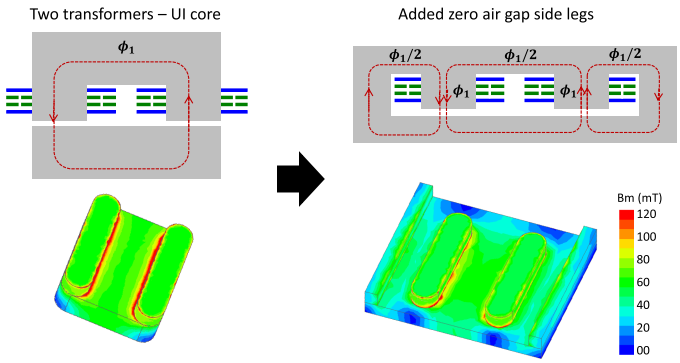

Fig. 35. Adding zero-air-gap side legs to the integrated two transformers in a UI core.

mean length and increases the winding loss. There is a tradeoff here between the core loss and winding loss. The core thickness d is swept at the same A_e, B_m, and total transformer footprint, as shown in Fig. 34(a). Fig. 34(b) shows the reduction in core loss as the thickness of the core reduces. The reduction in core loss is mainly due to eddy loss reduction, as depicted in Fig. 34(c). Reducing core thickness reduces eddy loss in the transformer legs and top and bottom plates as well. However, reducing the core thickness increases winding loss. An optimized core thickness is selected to get the least total transformer loss.

Further improvement can be made by further reducing the top and bottom plate thickness. A standard EI core or PQ core has less plate thickness than a UI core, thus reducing eddy loss. The eddy loss in the integrated two transformers can be reduced similarly by adding two low reluctance side legs with zero air gaps, as shown in Fig. 35. The side legs carry half the transformer

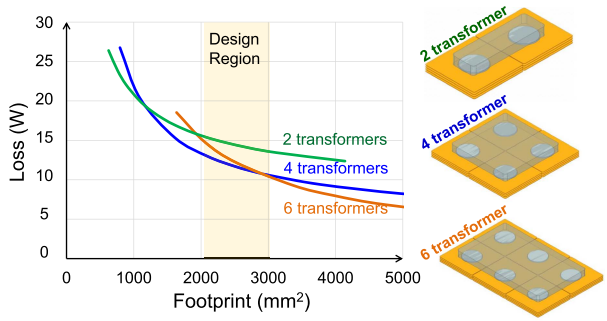

(a)

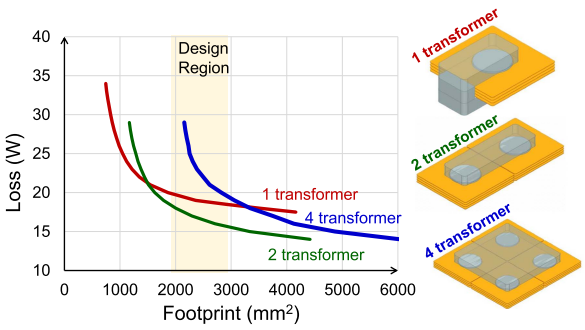

(b)

Fig. 36. Evaluation of different transformer numbers. (a) Without considering dimensional effects on the core, four transformers are the best option within the design region. (b) After considering the dimensional effects on the core, two transformers have the least loss with the design region.

flux, and the plates only carry half the flux [11]. To keep the same flux density in the plates as in the transformer legs, the plate thickness is reduced by 50%. The reduced plate thickness further reduces the plate's eddy loss, where the eddy loss is reduced from 1.6 W in the UI core to 1 W after adding the side legs. The better flux distribution provided by the added side legs also reduces the flux crowding at the corners between the legs and the plate. Another benefit is the lower profile magnetics and higher power density. These guidelines apply to all the planar magnetic components, including inductors. The resonant inductor of the LLC is designed similarly to reduce the inductor core loss.

VII. Experimental Results

The design concept is verified on a 1-MHz 3-kW 400-to-48-V LLC with planar magnetics. Two generations of the LLC converter are compared. The comparison aims to demonstrate two converters with the same specifications (input voltage, output voltage, power rating, and switching frequency) yet with different magnetic structures. Gen. 1 is designed without considering the dimensional effects in the core [7], which theoretically underestimate the core loss. Thus, four transformers are used because of the false assumption of low core loss, as shown in Fig. 36(a). On the other hand, Gen. 2 calculates the excess loss due to the dimensional effects, which resulted in a different conclusion that a two-transformer structure is more efficient, as shown in Fig. 36(a). The two-transformer structure is then improved using elongated thin cores with additional side legs to minimize the dimensional effects on the core loss. The prototype

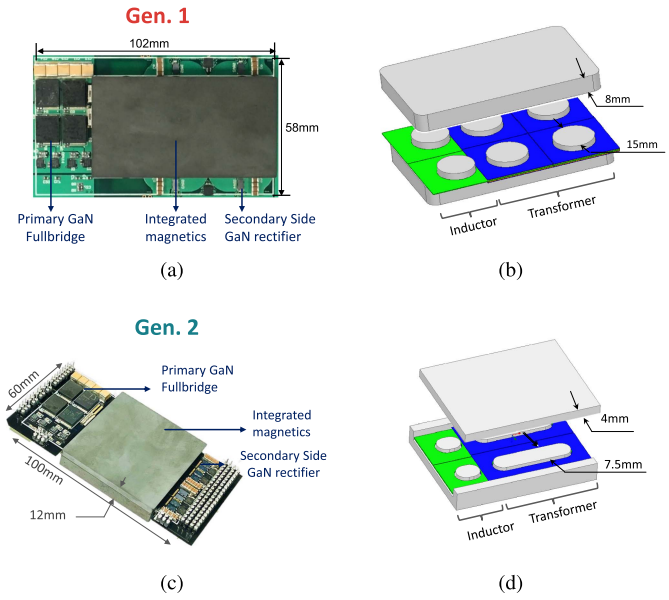

(a) (b) (c) (d)

Fig. 37. Implemented 1-MHz 3-kW LLC. (a) Gen. 1 prototype. (b) Gen. 1 magnetic design. (c) Gen. 2 prototype. (d) Gen. 2 magnetic design.

TABLE II
Prototype Parameters

Parameter	Generation 1	Generation 2
Input voltage	400 V	
Output voltage	40 V-60 V	
PCB	Six-layer, 2oz. Cu.	
Core Material	ML91S—Proterial	
Primary driver	Isolated Si8273	
Primary GaN device	IGT60R042D1 600V 42 mΩ	
SR driver	HB driver LMG5113	
Synch. Rectifier topology	center-tap	full-bridge
SR GaN device	EPC2033, 150V	EPC2029 80V
Magnetizing inductance	20 μH	22 μH
Resonant inductance	3.4 μH	4.3 μH
Resonant frequency	1 MHz	1 MHz
Switching frequency	890 kHz	880 kHz

of the two generations is shown in Fig. 37. The two converters (Gen. 1 and 2) use the same input full-bridge devices and the same number of output rectifiers. Therefore, the difference in the experimental losses between the two generations is primarily due to the magnetic design. The comparison demonstrates the importance of accurate core loss modeling for a better magnetic structure and design with experimental verification. The integrated magnetics, power switches, and driving circuits are populated on a six-layer PCB. The PCB-based transformer uses four layers for the windings and two for the shielding. The prototype information is listed in Table II.

The two converters use the same primary-side full-bridge inverter and four output rectifiers, and both run at 1-MHz resonant frequency. Therefore, the difference in performance is mainly due to magnetic performance. Gen. 2 can achieve higher peak efficiency of 98%, as shown in Fig. 38. This increase in peak efficiency compared to Gen. 1 is due to the reduced transformer

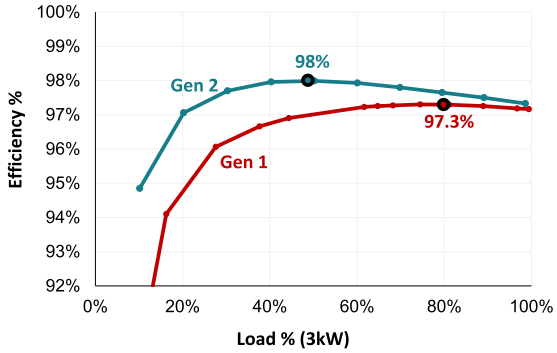

Fig. 38. Tested efficiency at 400-to-50 V.

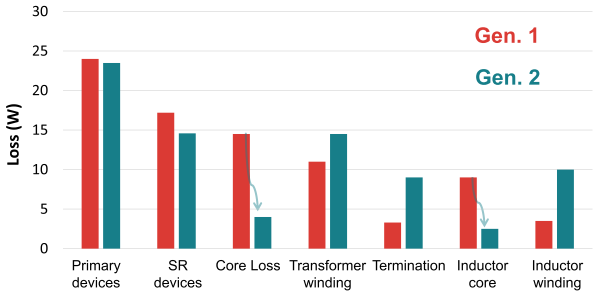

Fig. 39. Loss breakdown at full load.

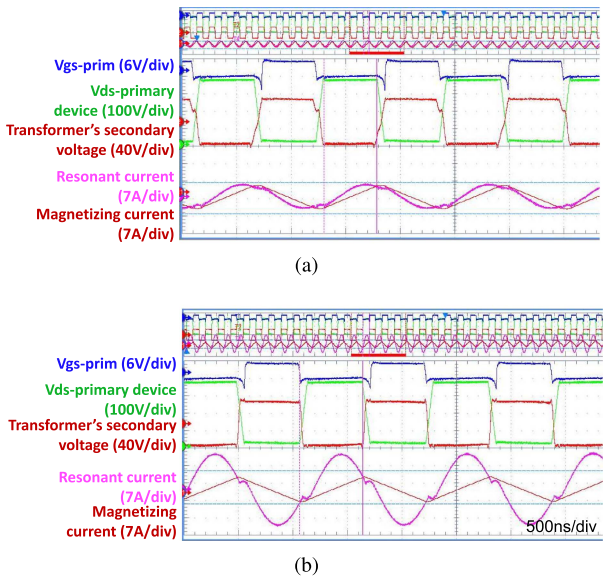

Fig. 40. Operating waveforms at nominal operation at 400-V input and 50-V output. (a) 20% load (12-A output current, 600-W power). (b) 100% load (60-A output current, 3000-W power).

core loss, as shown in Fig. 39, which is a fixed loss independent of output power in the LLC converter. The reduced transformer core loss offers higher light-load efficiency. The peak efficiency is located at 50% load, providing high average efficiency of around half-load, which is the most important for data center power supplies [37], [38], [39].

A tradeoff is made to reduce core loss as the winding loss in Gen. 2 increases. The increase in winding loss is due to the fewer number of elemental transformers as compared to Gen. 1.

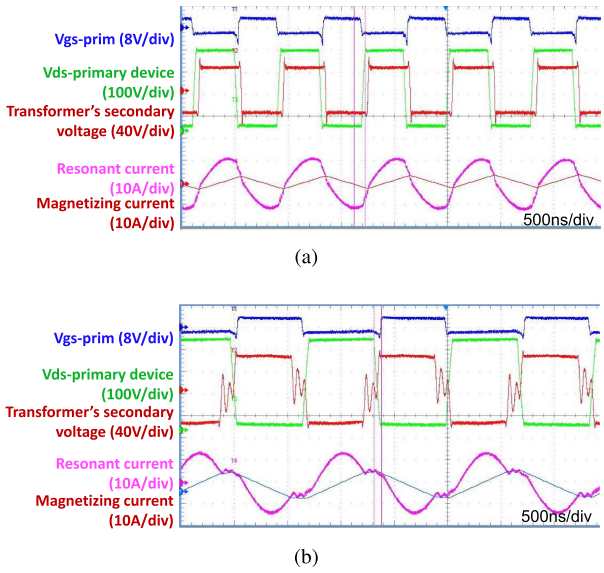

Fig. 41. Operating waveforms at full load. (a) 40-V, 62-A output. (b) 60-V, 50-A output.

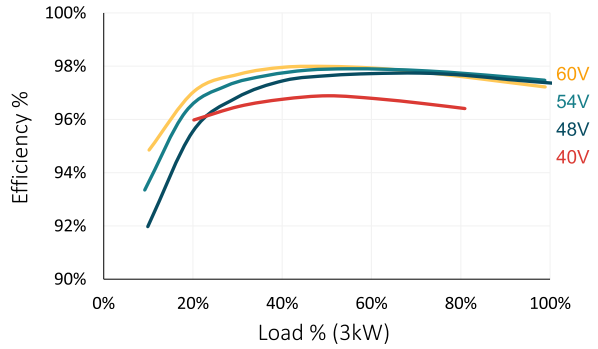

Fig. 42. Measured efficiency at different output voltages with 40–60 V range.

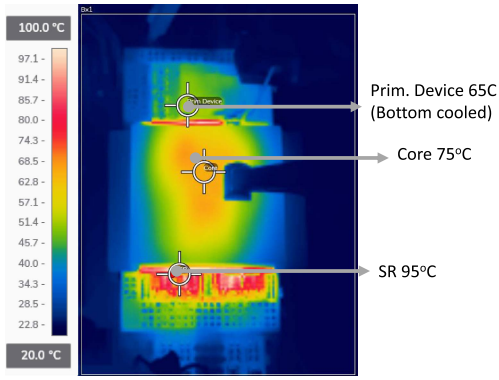

Fig. 43. Thermal performance of the 3-kW LLC converter with the forced air cooling of 600 LFM.

Also, the winding loss increases due to the use of the rectangular core shape, which increases the mean length of the transformer windings and increases the winding loss, as shown in Fig. 34(b). On the other hand, Gen. 1 uses a round core shape, which renders the least winding mean length but at the expense of higher core loss. For the inductor, the winding loss increased due to more inductor turns in Gen. 2 than in Gen. 1. Gen. 2 uses an eight-turn

TABLE III
SURVEY AND COMPARISON OF THE 400-TO-40–60 V REGULATED DC–DC CONVERTERS FOR 48-V DATA CENTER ARCHITECTURE

	This work	[18] 2019	[7] 2022	[12] 2020	[13], [14] 2021
Topology	Full-bridge LLC	Three-phase LLC	Full-bridge CLL	Half-bridge CLL	Full-bridge LLC
Rated power	3 kW	3 kW	3 kW	800 W	3.2 kW
Frequency	1 MHz	1 MHz	1 MHz	700 kHz	550 kHz
Implementation	PCB magnetics	PCB magnetics	PCB magnetics	PCB magnetics	Stacked PCB Tr., Litz wire L_r
Peak efficiency	98%	97.5%	97.3%	95.83%	98.6%
Power density	700 W/in^3	600 W/in^3	550 W/in^3	220 W/in^3	73 W/in^3*

*Calculated for the whole power supply unit (PFC + LLC).

inductor to reduce the inductor core size to avoid excess core loss, while Gen. 1 uses a four-turn inductor. The termination loss also increased in Gen. 2, which describes the loss in the connection between the secondary winding terminals and the rectifiers. While the number of rectifiers is kept the same (four rectifiers in Gen. 1 and 2), Gen. 2 uses only two transformers, as shown in Fig. 31; each transformer delivers 30 A. Such a high current creates a high loss in the PCB traces connecting the transformer's winding to the rectifier.

The measured efficiency excludes the gate loss. The gate drivers are supplied externally from a bench power supply. The gate driving losses are measured experimentally by calculating the output power of the drivers' supply. The primary driving loss is 0.8 W, and the secondary driving loss is 0.9 W. Since GaN devices are used on both primary and secondary sides, the driving losses are insignificant and combined are less than 2 W. GaN technology helps to maintain high efficiency at light load and idle mode by leveraging the low driving and switching losses.

Fig. 40 shows the steady-state operating waveforms of the 3-kW converter at the nominal operating point ($V_{\text{in}} = 400$ V, $V_o = 50$ V). At nominal operation, the converter runs close to the resonant frequency 1 MHz with a sinusoidal resonant current, rendering the LLC converter's best efficiency. The waveforms show the drain–source voltage of the primary switch (green), the transformer voltage on the secondary winding (red), the primary resonant current (magenta), and the magnetizing current (red). The magnetizing current is derived or calculated using the math function in the scope by integrating the secondary transformer voltage and dividing it by the magnetizing inductance. Fig. 40(a) shows the waveforms at 12-A output current and 600-W power. Fig. 40(b) shows the waveforms at 60-A output current and 3000-W power. Fig. 41 shows the operating waveforms at output voltages of 40 and 60 V and the output range for the 3-kW power supply according to the open compute project standard [40]. The converter uses frequency modulation to regulate the output voltage. At 60 V, the switching frequency is reduced to 740 KHz to boost the output voltage. At 40 V, the switching frequency is increased to 1.26 MHz to step down the output voltage. The converter achieves zero-voltage switching at all the operating conditions for primary and secondary devices and near zero-current switching for the synchronous rectifier. The efficiency is tested at the whole output voltage range, as shown in Fig. 42. The converter maintains peak efficiency at 98% at the output voltage of 48–60 V. The lowest efficiency is 97% and happens at 40 V, which is the worst case due to the high output current and high switching frequency.

Fig. 43 shows the steady-state thermal performance of the 3-kW prototype in the case of full power and 600 LFM forced air cooling. The hot spot appears at the secondary rectifier of 95 °C, and the core temperature is 75 °C. Better thermal management can be achieved by using a combination of a heat spreader and a heat sink to cool the secondary-side rectifier [41].

This work is compared to the state-of-the-art achievements in the regulated 400-to-40–60 V converters for the Open Rack V2 power supply [40], as shown in Table III. The proposed 3-kW LLC converter shows superiority in terms of implementation, efficiency, and power density. The proposed converter achieved the highest power density of 700 W/in^3 and efficiency of 98% in the 1-MHz converter class. This is achieved thanks to the careful design of the core loss by accounting for the dimensional effects. Later designs based on the latest Open Rack V3 power supply [42] have shown further improvement in efficiency due to the reduced regulation range [43].

VIII. CONCLUSION

For high-frequency (>1 MHz) and high-power (>3 KW) applications, unexpected core loss is observed due to dimensional resonance and skin effect. This is especially true for a planar PCB-based magnetic structure. In conventional practice, dimensional effects are usually observed with an oversized core; however, for high-frequency ferrite material, it can be an important core loss factor in a core size considered normal. These unwanted dimensional effects are evaluated using an FEA tool for accounting for the true core losses. This will be especially helpful for irregular core shapes of planar low-profile integrated magnetics. The accurate modeling of core loss in FEA requires an accurate characterization of ferrite material conductivity and permittivity to account for eddy loss and dimensional resonance; this is not readily available for this new generation of high-frequency material. The technique for measuring the complex conductivity and permittivity is first introduced. Then, the nonlinear permeability and dimensional resonance are quantified both analytically and experimentally. Design practices and guidelines minimizing the dimensional effects are developed. Special attention is given to designing low-profile planer integrated magnetics with an emphasis on uniform flux distribution. Reduction of the core thickness is critical to reducing the dimensional effects, thus reducing eddy loss. Such a design practice is demonstrated on a 3-kW 1-MHz LLC converter. By using an elongated thin core shape at 1 MHz, the efficiency improved from 97.3% to 98% due to the reduction in core loss.

ACKNOWLEDGMENT

The authors would like to thank Hitachi Metals, Hengdian Group DMEGC Magnetics, and ACME for in-kind donations of ferrite samples. The authors would also like to thank Infineon for in-kind donations of 600-V GaN samples.

REFERENCES

[1] E. M. Bibra et al., "Global EV outlook 2022: Trends in charging infrastructure," Int. Energy Agency, Paris, France, Tech. Rep., 2022. [Online]. Available: https://www.iea.org/reports/global-ev-outlook-2022

[2] N. Jones, "How to stop data centres from gobbling up the world's electricity," *Nature*, vol. 561, no. 7722, pp. 163–167, 2018.

[3] I. Aghabali, J. Bauman, P. J. Kollmeyer, Y. Wang, B. Bilgin, and A. Emadi, "800-V electric vehicle powertrains: Review and analysis of benefits, challenges, and future trends," *IEEE Trans. Transpt. Electrific.*, vol. 7, no. 3, pp. 927–948, Sep. 2021.

[4] X. Li and S. Jiang, "Google 48 V power architecture," in *Proc. IEEE Appl. Power Electron. Conf. Expo.*, 2017.

[5] F. C. Lee, Q. Li, and A. Nabih, "High frequency resonant converters: An overview on the magnetic design and control methods," *IEEE Trans. Emerg. Sel. Topics Power Electron.*, vol. 9, no. 1, pp. 11–23, Feb. 2021.

[6] F. Jin, A. Nabih, C. Chen, X. Chen, Q. Li, and F. C. Lee, "A high efficiency high density DC/DC converter for battery charger applications," in *Proc. IEEE Appl. Power Electron. Conf. Expo.*, 2021, pp. 1767–1774.

[7] A. Nabih, Q. Li, and F. C. Lee, "Magnetic integration of four-transformer matrix with high controllable leakage inductance using a five-leg magnetic," in *Proc. IEEE Appl. Power Electron. Conf. Expo.*, 2022, pp. 693–700.

[8] C. Fei, F. C. Lee, and Q. Li, "High-efficiency high-power-density LLC converter with an integrated planar matrix transformer for high-output current applications," *IEEE Trans. Ind. Electron.*, vol. 64, no. 11, pp. 9072–9082, Nov. 2017.

[9] G. R. Skutt, "High-frequency dimensional effects in ferrite-core magnetic devices," Ph.D. dissertation, Dept. Elect. Comput. Eng., Virginia Polytechnic Inst. State Univ., Blacksburg, VA, USA, 1996.

[10] Z. Yi, K. Sun, S. Lu, G. Cao, Y. Li, and J.-I. Ha, "High-precision simulation for structure and efficiency optimization of high-power high-frequency transformer," in *Proc. IEEE Energy Convers. Congr. Expo.*, 2020, pp. 3524–3531.

[11] K. D. Ngo, E. Alpizar, and J. K. Watson, "Modeling of losses in a sandwiched-winding matrix transformer," *IEEE Trans. Power Electron.*, vol. 10, no. 4, pp. 427–434, Jul. 1995.

[12] Y. Liu, H. Wu, Y. Tai, J. Zou, and Y. Jia, "Optimal design of GaN and PCB-winding based transformer-inductor-integrated magnetics for CLL resonant converter," in *Proc. IEEE Energy Convers. Congr. Expo.*, 2020, pp. 5430–5435.

[13] R. Yu, Q. Huang, T. Chen, A. Q. Huang, and T. Ribarich, "High-frequency and high-density design of all GAN power supply unit," in *Proc. Int. Exhib. Conf. Power Electron., Intell. Motion, Renewable Energy Energy Manage.*, 2018, pp. 1–5.

[14] R. Yu, T. Chen, P. Liu, and A. Q. Huang, "A 3-D winding structure for planar transformers and its applications to LLC resonant converters," *IEEE Trans. Emerg. Sel. Topics Power Electron.*, vol. 9, no. 5, pp. 6232–6247, Oct. 2021.

[15] F. G. Brockman, P. Dowling, and W. G. Steneck, "Dimensional effects resulting from a high dielectric constant found in a ferromagnetic ferrite," *Phys. Rev.*, vol. 77, no. 1, 1950, Art. no. 85.

[16] G. R. Skutt and F. C. Lee, "Characterization of dimensional effects in ferrite-core magnetic devices," in *Proc. 27th Annu. IEEE Power Electron. Spec. Conf.*, 1996, vol. 2, pp. 1435–1440.

[17] M. Kacki, M. S. Ryłko, J. G. Hayes, and C. R. Sullivan, "Analysis and experimental investigation of high-frequency magnetic flux distribution in Mn-Zn ferrite cores," *IEEE Trans. Power Electron.*, vol. 38, no. 1, pp. 703–716, Jan. 2023.

[18] C. Fei, R. Gadelrab, Q. Li, and F. C. Lee, "High-frequency three-phase interleaved LLC resonant converter with GaN devices and integrated planar magnetics," *IEEE Trans. Emerg. Sel. Topics Power Electron.*, vol. 7, no. 2, pp. 653–663, Jun. 2019.

[19] P. M. Gradzki, *Core Loss Characterization and Design Optimization of High-Frequency Power Ferrite Devices in Power Electronics Applications*. Blacksburg, VA, USA: Virginia Polytechnic Inst. State Univ., 1992.

[20] A. Nabih, R. Gadelrab, P. R. Prakash, Q. Li, and F. C. Lee, "High power density 1 MHz 3 kW 400 V-48 V LLC converter for datacenters with improved core loss and termination loss," in *Proc. IEEE Appl. Power Electron. Conf. Expo.*, 2021, pp. 304–309.

[21] W. Roshen, "Ferrite core loss for power magnetic components design," *IEEE Trans. Magn.*, vol. 27, no. 6, pp. 4407–4415, Nov. 1991.

[22] "Standard Test Methods for AC Loss Characteristics and Permittivity (Dielectric Constant) of Solid Electrical Insulation," ASTM Standard D150-18, 2022.

[23] M. Kacki, M. S. Ryłko, J. G. Hayes, and C. R. Sullivan, "Measurement methods for high-frequency characterizations of permeability, permittivity, and core loss of Mn-Zn ferrite cores," *IEEE Trans. Power Electron.*, vol. 37, no. 12, pp. 15152–15162, Dec. 2022.

[24] Z. Yi, K. Sun, H. Liu, and Q. Zhang, "Reduction methodology of eddy losses in ferrite cores for high-frequency transformers based on loss-effective conductivity extraction," in *Proc. IEEE Energy Convers. Congr. Expo.*, 2022, pp. 1–8.

[25] M. Mu, F. C. Lee, Q. Li, D. Gilham, and K. D. Ngo, "A high frequency core loss measurement method for arbitrary excitations," in *Proc. 26th Annu. IEEE Appl. Power Electron. Conf. Expo.*, 2011, pp. 157–162.

[26] D. Hou, M. Mu, F. C. Lee, and Q. Li, "New high-frequency core loss measurement method with partial cancellation concept," *IEEE Trans. Power Electron.*, vol. 32, no. 4, pp. 2987–2994, Apr. 2017.

[27] C. Tu, K. Ngo, and R. Chen, "A fast non-iterative design approach of one-turn inductor with significant AC flux using commercially available components," in *Proc. IEEE Appl. Power Electron. Conf. Expo.*, 2022, pp. 1486–1491.

[28] Z. Li, Y.-H. Hsieh, Q. Li, F. C. Lee, and M. H. Ahmed, "High-frequency transformer design with high-voltage insulation for modular power conversion from medium-voltage AC to 400-V DC," in *Proc. IEEE Energy Convers. Congr. Expo.*, 2020, pp. 5053–5060.

[29] N. He, M. Chen, J. Wu, N. Zhu, and D. Xu, "20-kW zero-voltage-switching SiC-MOSFET grid inverter with 300 kHz switching frequency," *IEEE Trans. Power Electron.*, vol. 34, no. 6, pp. 5175–5190, Jun. 2019.

[30] L. Wang, D. Zhang, J. Duan, and R. Gu, "Research on high performance multi-phase DC-DC converter applied to distributed electric propulsion aircraft," *IEEE Trans. Transp. Electrific.*, early access, doi: 10.1109/TTE.2022.3207142.

[31] H. N. Tran, T.-T. Le, H. Jeong, S. Kim, H.-P. Kieu, and S. Choi, "High power density DC-DC converter for 800 V fuel cell electric vehicles," in *Proc. IEEE 12th Energy Convers. Congr. Expo.—Asia*, 2021, pp. 2224–2228.

[32] A. Nabih, R. Gadelrab, Q. Li, and F. C. Lee, "Dimensional effects of core loss and design considerations for high frequency magnetics," in *Proc. IEEE Energy Convers. Congr. Expo.*, 2021, pp. 5488–5495.

[33] G. Elmen, "Magnetic properties of perminvar," *J. Franklin Inst.*, vol. 206, no. 3, pp. 317–338, 1928.

[34] A. Paduraru, M. Feder, and O. Caltun, "Magnetic properties of some perminvar ferrites," *J. Optoelectron. Adv. Mater.*, vol. 5, no. 4, pp. 945–950, 2003.

[35] D. J. Griffiths, *Introduction to Electrodynamics*. London, U.K.: Pearson, 2013.

[36] D. Reusch and F. C. Lee, "High frequency bus converter with low loss integrated matrix transformer," in *Proc. 27th Annu. IEEE Appl. Power Electron. Conf. Expo.*, 2012, pp. 1392–1397.

[37] K. M. U. Ahmed, M. Alvarez, and M. H. Bollen, "A novel reliability index to assess the computational resource adequacy in data centers," *IEEE Access*, vol. 9, pp. 54530–54541, 2021.

[38] D. Schall, V. Höfner, and M. Kern, "Towards an enhanced benchmark advocating energy-efficient systems," in *Proc. Technol. Conf. Perform. Eval. Benchmarking*, 2011, pp. 31–45.

[39] X. Zhang, J. Lu, and X. Qin, "BFEPM: Best fit energy prediction modeling based on CPU utilization," in *Proc. IEEE 8th Int. Conf. Netw., Archit. Storage*, 2013, pp. 41–49.

[40] "Open Rack Standard V2.0," *Open Compute Project*, Austin TX, USA, 2016.

[41] "Thermal Management of eGaN FETs," *Efficient Power Convers.*, El Segundo, CA, USA, 2021.

[42] "Open Rack V3 48 V Rectifier PSU Spec," *Open Compute Project*, Austin TX, USA, 2020.

[43] A. Nabih and Q. Li, "Design of 98.8% efficient 400V-48 V LLC converter with optimized matrix transformer and matrix inductor," *IEEE Trans. Power Electron.*, vol. 38, no. 6, pp. 7207–7225, Jun. 2023.

Ahmed Nabih (Member, IEEE) received the B.Sc. and M.Sc. degrees from Cairo University, Cairo, Egypt, in 2014 and 2017, respectively, and the Ph.D. degree from Virginia Tech, Blacksburg, VA, USA, in 2023, all in electrical engineering.

He is currently a Systems Engineer with Texas Instruments Inc., Dallas, TX, USA. His current research interests include wide-bandgap technology, high-power drivers, digital control, high-frequency resonant converter design, and planar magnetics.

Dr. Nabih was the recipient of the Best Paper Award of the OCP Future Technology Symposium in 2020 and multiple APEC outstanding presentation awards.

Feng Jin (Student Member, IEEE) received B.Sc. and M.Sc. degrees in electrical engineering from the Nanjing University of Aeronautics and Astronautics, Nanjing, China, in 2012 and 2015, respectively. He is currently working toward the Ph.D. degree in electrical engineering with the Center for Power Electronics Systems, Virginia Tech, Blacksburg, VA, USA.

His current research interests include EV charging, bidirectional power conversion, and planar magnetics.

Rimon Gadelrab (Member, IEEE) received B.Sc. and M.Sc. degrees from Alexandria University, Alexandria, Egypt, in 2012 and 2015, respectively, and the Ph.D. degree from Virginia Tech, Blacksburg, VA, USA, in 2023, all in electrical engineering.

He is currently an Application Engineer with Texas Instrument Inc., Dallas, TX, USA. His current research interests include high-frequency, high power density, and high-efficiency power conversion.

Fred C. Lee (Life Fellow, IEEE) received the B.S. degree from National Cheng Kung University, Tainan City, Taiwan, in 1968, and the M.S. and Ph.D. degrees from Duke University, Durham, NC, USA, in 1972 and 1974, respectively, all in electrical engineering.

He is currently a University Distinguished Professor Emeritus with Virginia Polytechnic Institute and State University (Virginia Tech), Blacksburg, VA, USA, and the Founder and Director Emeritus of the Center for Power Electronics Systems, an engineering research center consisting of 80 corporations. His research interests include high-frequency power conversion, magnetics and EMI, distributed power systems, high-density electronics packaging and integration, and modeling and control. He holds 105 U.S. patents, and has authored or coauthored more than 335 journal articles and more than 780 refereed technical papers. During his tenure with Virginia Tech, he has supervised to completion 90 Ph.D. and 93 master's students.

Dr. Lee was the President of the IEEE Power Electronics Society (1992–1994) and was the recipient of the William E. Newell Power Electronics Award in 1989; PCIM Award for Leadership in Power Electronics Education presented at HFPC in 1990; the Arthur E. Fury Award for Leadership and Innovation in 1998; the Honorary Sun Yuen Chuan Chair Professor of National Tsing Hua University in Taiwan in 2001; the Ernst-Blickle Award sponsored by SEW-EURODRIVE Foundation in 2005; the Distinguished Alumni Award from National Cheng Kung University in 2006; the Honorary Li Kwoh-Ting Chair Professor of National Cheng Kung University in 2011; the Inaugural Member of the Virginia Tech Entrepreneur Hall of Fame in 2012; the Honorary Chair Professor of National Chiao Tung University in Taiwan in 2014; the IEEE Medal in Power Engineering "for contributions to power electronics, especially high-frequency power conversion," in 2015; the Power Supply Technology Outstanding Achievement Award from China Power Supply Society (CPSS) in 2017; the Honorary Chair Professor of Tsinghua University in China in 2017; and the Honorary Professor of Huazhong University of Science and Technology in China in 2018. He is a Member of the U.S. National Academy of Engineering, an Academician of the Academia Sinica in Taiwan, and a Foreign Member of the Chinese Academy of Engineering in the People's Republic of China. He was elected as National Academy of Inventors (NAI) Fellow in 2018, and endorsed in 2019 as a Leader in engineering and education with the Albert Nelson Marquis Lifetime Achievement Award.

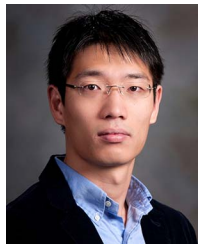

Qiang Li (Member, IEEE) received the B.S. and M.S. degrees in power electronics from Zhejiang University, Hangzhou, China, in 2003 and 2006, respectively, and the Ph.D. degree in electrical engineering from Virginia Tech, Blacksburg, VA, USA, in 2011.

He is currently an Associate Professor with the Center for Power Electronics Systems, Virginia Tech. He holds 37 U.S. patents and has authored or coauthored 185 refereed technical articles. His current research interests include power management for distributed power systems, applications of wide-bandgap power devices, high-frequency power conversion and controls, magnetics and electromagnetic interference, high-density electronics packaging and integration, and renewable energy.

Dr. Li was the recipient of the First Place Prize Article Award of IEEE Transactions on Power Electronics in 2016 and the 2017 U.S. National Science Foundation Career Award.